Aalto University
School of Science

Jukka-Pekka Kaikkonen

Role of Atmospheric Boundary Layer Processes in the Diurnal Evolution of CO_2 Concentration

Master's thesis submitted in partial fulfillment of the requirements for the degree of Master of Science in Technology.

Espoo, March 8, 2012

Supervisor: Prof. Mikko Alava
Instructor: Prof. David Pino

Aalto University
School of Science

Abstract of Master's thesis

Author:	Jukka-Pekka Kaikkonen
Degree programme:	Degree Programme in Engineering Physics
Major subject:	Engineering physics
Minor subject:	Mathematics
Title:	Role of Atmospheric Boundary Layer Processes in the Diurnal Evolution of CO_2 concentration
Title in Finnish:	Ilmakehän rajakerrosprosessien rooli CO_2-konsentraation diurnaalisessa kehityksessä
Chair:	Tfy-3 Physics
Supervisor:	Prof. Mikko Alava
Instructor:	Prof. David Pino

Abstract:

Atmospheric boundary layer (ABL) is the lower portion of the troposphere that links the biosphere and atmosphere by exchanging heat, moisture, carbon dioxide (CO_2) and other constituents between them. Interpretation of observed CO_2 mixing ratios in the ABL require information of the dynamical characteristics of the ABL. Horizontal advection and large scale subsidence are however rather difficult to measure and often their contribution on the ABL budget cannot be conclusively addressed. This causes significant uncertainties on the estimates of biosphere-atmosphere CO_2 exchange that is inferred from the CO_2 mixing ratio observations. This Master's Thesis examines the influence of horizontal CO_2 advection and large scale subsidence on the diurnal evolution of CO_2 mixing ratio in a convective ABL. From a conceptual mixed-layer theory, a set of analytical sensitivity equations is derived to quantify the contribution of horizontal CO_2 advection and other ABL variables on the bulk CO_2 mixing ratio evolution. Similar equations are also derived for the inferred biosphere-atmosphere CO_2 exchange.

Measurements during two well characterized convective days at the Cabauw tower in the Netherlands are analyzed by using the derived relations. This analysis shows that errors in horizontal CO_2 advection can lead to notable uncertainties in the diurnal evolution of the CO_2 mixing ratio and the inferred CO_2 surface exchange. Moreover, a systematic study is performed to investigate the behaviour of the derived sensitivities on different days by changing the initial vertical profiles of potential temperature and CO_2 mixing ratio in the mixed-layer simulations.

Influence of large scale subsidence on the diurnal evolution of CO_2 mixing ratio and the inferred CO_2 surface exchange is demonstrated by numerical mixed-layer simulations. These simulations indicate that an erroneous large scale subsidence can also cause non-negligible uncertainties in the evolution of the CO_2 mixing ratio and the inferred CO_2 surface exchange. The results presented in this thesis hence implicate that horizontal advection and large scale subsidence should be carefully regarded also when processes on diurnal time scales are considered.

Date: March 8, 2012	Language: English
Number of pages: 58	Keywords: carbon dioxide, atmosphere, boundary layer, advection

Aalto Yliopisto
Perustieteiden korkeakoulu

Diplomityön tiivistelmä

Tekijä:	Jukka-Pekka Kaikkonen
Koulutusohjelma:	Teknillisen fysiikan koulutusohjelma
Pääaine:	Teknillinen fysiikka
Sivuaine:	Matematiikka
Työn nimi:	Ilmakehän rajakerrosprosessien rooli CO_2-konsentraation diurnaalisessa kehityksessä
English title:	Role of Atmospheric Boundary Layer Processes in the Diurnal Evolution of CO_2 Concentration
Professuurin koodi ja nimi:	Tfy-3 Fysiikka
Työn valvoja:	Prof. Mikko Alava
Työn ohjaaja:	Prof. David Pino

Tiivistelmä:

Ilmakehän rajakerros on troposfäärin alin kerros, joka yhdistää biosfäärin ja ilmakehän siirtämällä lämpöä, kosteutta, hiilidioksidia (CO_2) ja muita ainesosia niiden välillä. Mitattujen hiilidioksidipitoisuuksien tulkinta vaati tietoa ilmäkehän rajakerroksen dynaamisista ominaisuuksista. Horisontaalisen hiilidioksidin (CO_2) advektion ja suuren mittakaavan vajoamisen mittaaminen on kuitenkin varsin hankalaa ja usein niiden kontribuutiota ilmakehän rajakerroksen budjettiin ei voida pitävästi osoittaa. Tämä aiheuttaa merkittävää epävarmuutta havaittujen CO_2-pitoisuuksien avulla pääteltyihin arvioihin biosfäärin ja ilmakehän välisestä CO_2-vaihdosta. Tämä diplomityö tarkastelee horisontaalisen CO_2:n advektion ja laajan mittakaavan vajoamisen vaikutusta CO_2-konsentaarion diurnaaliseen kehitykseen konvektiivisessa ilmakehän rajakerroksessa. Konseptuaalisesta sekoittuneen kerroksen teoriasta johdetaan joukko analyyttisiä sensitiivisyysyhtälöitä, jotka määrittävät horisontaalisen CO_2:n advektion ja muiden ilmakehän rajakerrosta kuvaavien muuttujien kontribuution CO_2-konsentraation kehityksessä.

Kahden konvektiivisen päivän mittaustulokset Cabauwn mastolta Alankomaista analysoidaan johdettuja relaatioita käyttäen. Tämä analyysi osoittaa, että tyypilliset virheet horisontaalisessa advektiossa johtavat huomattaviin epämääräisyyksiin sekä CO_2-pitoisuuksissa että päätellyissä pinnan CO_2-vaihdossa. Lisäksi johdettujen sensitiivisyyksien käyttäytymistä tutkitaan systemaattisesti erilaisina päivinä muuttamalla alun potentiaalilämpötilan ja CO_2-pitoisuuden vertikaalisia profiileja sekoittuneen kerroksen simulaatioissa.

Laajan mittakaavan vajoamisen vaikutus CO_2-pitoisuuden ja päätellyn CO_2-vaihdon diurnaaliseen kehitykseen havainnollistettiin numeerisilla sekoittuneen kerroksen simulaatioilla. Nämä simulaatiot osoittavat, että virheellinen laajan mittakaavan vajoaminen voi myös johtaa merkittäviin epämääräisyyksiin CO_2-pitoisuuksien ja päätellyn CO_2-vaihdon kehityksessä. Tässä diplomityössä esitetyt tulokset siten merkitsevät, että horisontaalinen advektio ja laajan mittakaavan vajoaminen on huolellisesti huomioitava myös diurnaalisen aikaskaalan prosesseja tarkasteltaessa.

Päivämäärä: 8.3.2012	Kieli: Englanti
Sivumäärä: 58	Avainsanat: hiilidioksidi, ilmakehä, pintakerros, advektio

Acknowledgements

This Master's thesis was done under instruction of professor David Pino in the Universitat Politècnica de Catalunya. The work has been partly funded by the Spanish MICINN CGL2009-08609 and INTERREG EU FLUXPYR EFA 34/08 projects.

I wish to thank professor David Pino for providing me the opportunity to do my Master's thesis under his instruction. I am also grateful for his help with many practical issues in Barcelona and his support during the thesis work. Moreover, I would like to acknowledge Fred Bosveld of the Royal Netherlands Meteorological Institute (KNMI) and Alex Vermeulen of the Energy Research Center of The Netherlands (ECN) for the observational data, and Supercomputing Center of Catalonia (CESCA) for the computational resources. I would like to thank professor Mikko Alava for supervising this thesis. Finally, I would like to express my gratitude to my family for the continuous encouragement and support during my student years.

Accra, February 20, 2012

Jukka-Pekka Kaikkonen

Contents

Chapter 1

Introduction

1.1 Atmospheric boundary layer

Atmospheric boundary layer (ABL), or planetary boundary layer, is the lower portion of the troposphere that is directly affected by the Earth's surface on a timescale of about 30 minutes or less [1, 2]. It is only a shallow portion of the whole atmosphere but in this part most of us spend all of our lives and our perception of the atmosphere is largely based on the characteristics of this layer.

Earth's surface has a dominating influence on the ABL. Surface forcings like frictional drag, evaporation, transpiration, heating and terrain induced flow modification influence the ABL dynamics. Turbulence is the dominating transport process in the ABL which allows the ABL to respond to surface forcings relatively fast. Due to large diurnal variation of surface forcings and due to ABL's quick response to surface characteristics, the ABL exhibits a large diurnal variation of wind, moisture, heat and pollutants.

ABLs can be divided into two main types which are convective boundary layers (CBL) and stable boundary layers. CBLs, which are considered in this thesis, are dominated by buoyancy driven turbulence. Positive buoyancy fluxes are caused by positive sensible heat and latent heat surface fluxes which are induced by solar radiation. Buoyant turbulent fluxes are iniated in a surface layer which is roughly 5 to 10% of the CBL depth [3]. Above the surface layer buoyancy driven turbulence is often arranged into large thermals and plumes of warm air rising from the ground. These thermals are illustrated in Figure 1.1 which shows vertical cross sections of vertical velocity and specific humidity perturbations obtained from a large-eddy simulation of the CBL. This turbulence tends to mix the air giving rise to almost constant vertical profiles of potential temperature, specific humidity and mixing ratio of inert scalars in the middle of the CBL during the day. This middle part of the CBL is called the mixed-layer (ML) and it accounts for 35 to 85% of the whole CBL depth.

At the top of the CBL rising thermals encounter the free atmosphere (FA) with warmer air and less turbulence. Therefore, the thermals become negatively buoyant and they sink back down into the ML. These thermals however overshoot shortly into the FA and mix down some air from the FA into the ML. This mixing of FA air into the ML is called entrainment and it is partially responsible for the growth of CBL during the day. The region where entrainment occurs is

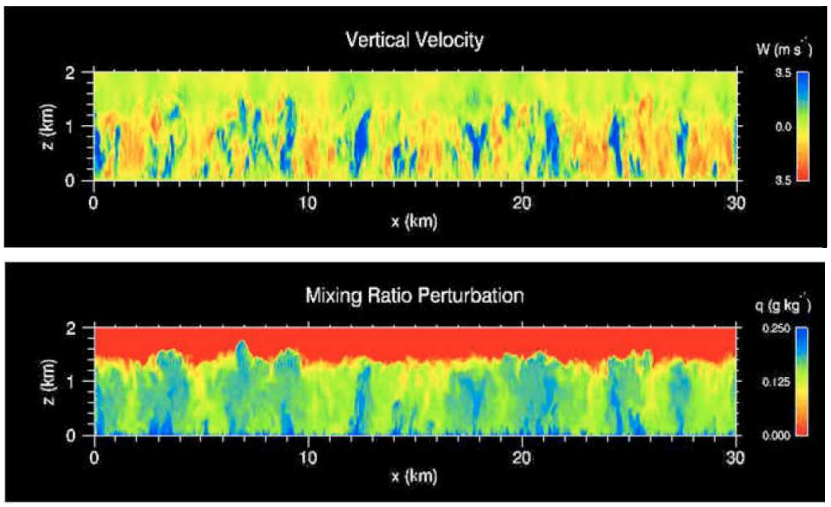

Figure 1.1: Vertical cross sections of vertical velocity and specific humidity perturbations in the convective boundary layer obtained from a large-eddy simulation. Courtesy of Peter Sullivan (NCAR).

called entrainment zone or inversion layer and it composes the rest 10 to 60% of the CBL depth. Atmosheric variables change strongly across the entrainment zone and sometimes absolute temperature can even increase with height within this layer. This inversion layer separates the CBL from the FA and in clear sky conditions it keeps most of the heat, moisture and pollutants released near the ground inside the CBL. CBL processes therefore play a dominant role in the day time evolution of heat, moisture and pollutants.

When the surface fluxes decreases after midday, turbulence in the ML starts to decay. The resultant layer of air is called residual layer since its mean state variables remain the same as in the just decayed ML. The ground continues to cool after sunset cooling the air adjacent to it. The layer below the residual layer becomes statistically stable damping the turbulent motion. This layer is called stable boundary layer and it is driven by the wind shear turbulence and the stabilization effects due to radiative cooling. It occurs over land during night so it is also known as nocturnal boundary layer.

1.2 Biosphere-atmosphere CO_2 exchange

Carbon dioxide concentrations in the atmosphere have risen significantly after the industrial revolution [4, 5]. Elevated CO_2 concentrations have drawn a lot of attention among the scientists and policy makers since CO_2 is a greenhouse gas and consequently, is connected to the global climate change [6–9]. Atmospheric CO_2 content is increased by anthropogenic and natural sources of CO_2 and decreased by biospheric and oceanic sinks of CO_2. The growing trend of atmospheric CO_2 therefore suggests an imbalance between the sources and sinks of CO_2 but the details of this whole process are not yet accurately known. Atmospheric CO_2 concentration also exhibits large interannual variability which

is not well understood yet [10]. Moreover, by changing the radiative balance of the atmosphere, the increase in the CO_2 concentration and other greenhouse gases also modify the water cycle and oceanic circulations. To identify different sources and sinks of CO_2 and their contribution to the global carbon cycle, significant efforts have been put in to the estimation of CO_2 exchange between the biosphere and the atmosphere on different time and length scales.

Numerous methods have been used to obtain information about the biosphere-atmosphere CO_2 exchange. Eddy-covariance method measures directly fluxes of CO_2, water vapour and energy, and it is used on a global network of micrometeorological flux measurement sites [10–12]. The flux data considered in this thesis is gathered from one of these eddy-covariance measurement sites. Direct eddy-covariance measurements can be also performed by mounting the instruments on an airplane [13, 14]. This increases the spatial coverage of the measurements but cannot be employed continuously on long time scales. Most other methods determine exchange fluxes indirectly from the observed CO_2 mixing ratios. This is done by boundary layer budget methods [15] or by atmospheric tracer transport models [16–20]. However, both methods have some disadvantages and they show largely variable agreement when compared to the direct methods [21]. Atmospheric transport plays an important role in the inverse methods and thus their success strongly depend on the accuracy of the decribed atmospheric transport.

As it was already mentioned, most of the carbon dioxide released during daytime near the ground stays in the CBL due to the inversion layer separating the CBL and the FA. Consequently, surface turbulent fluxes and CBL dynamics strongly influences the exchange of CO_2 between the CBL and the surface [10, 22, 23], and between the CBL and the FA [24–29]. Correspondingly, they also affect the vertical and horizontal distribution of CO_2 in the atmosphere [30, 31]. Accurate CBL modeling is therefore crucial for forward simulations of CO_2 mixing ratios based on the measured CO_2 surface fluxes, and for inferring CO_2 surface fluxes from the observed CO_2 mixing ratios. It is thus important to quantify the influence of CBL dynamics on the CO_2 mixing ratio, and on the inferred CO_2 surface flux [22]. Pino *et al.* [32] approached this issue by using conceptual mixed-layer model (MLM) [33–37] which gives an analytical equation for the diurnal evolution of CO_2 mixing ratio in the CBL. From this equation they derived a set of sensitivity equations which are able to quantify the uncertainties in the CO_2 mixing ratio due to errors in different CBL variables.

Pino *et al.* excluded horizontal and vertical advection of CO_2 in their analysis [32]. Accurate measurement and modeling of advection is generally quite difficult so the uncertainties in the estimated advection can be relatively large. Consequently, this could lead to non-negligible errors in the simulated CO_2 mixing ratios, and in the inferred CO_2 surface fluxes. In this thesis the framework of Pino *et al.* is extended to include horizontal advection of CO_2. MLM cannot describe vertical advection inside the CBL since it assumes vertically uniform CO_2 distribution in the CBL. The influence of large scale subsidence on the exchange of CO_2 between the CBL and the FA can be nevertheless considered with the MLM. Analytical equations for this influence is not obtained but the effect of subsidence is demonstrated by numerical experiments.

1.3 Outline of the thesis

This thesis considers the contribution of horizontal advection and large scale subsidence on the diurnal evolution of CO_2 mixing ratio by using a conceptual MLM [33–37]. The following chapter first introduces the basic thermodynamical definitions and equations that are relevant in this thesis. MLM is then described in detail since it is the central model that is used in the thesis. The fifth-generation Pennsylvania State University - National Center of Atmospheric Research Mesoscale Model (MM5) [38] is described only shortly since it is just used as a supplementary tool in the thesis.

In chapter 3 the sensitivity equations are derived from the MLM equations. Chapter 4 provides description of the measurements that are later used to demonstrate the capability of MLM to simulate an observed diurnal evolution of CBL during two selected days. In chapter 5 diurnal CBL evolution of these days is first simulated with MLM. Sensitivity analysis developed in chapter 3 is then applied to these days. Furthermore, the influence of subsidence on the simulated CO_2 mixing ratios is considered. The selected days have been analyzed in previous publications [28, 32] but some new insights are given about the meteorological conditions on the second day. Finally, chapter 6 draws the conclusions about the work. The limitations of the framework is also discussed and some future outlooks are mentioned.

Chapter 2

Theory and models

This chapter provides the description of the models and theory used in this thesis. Definitions of the main thermodynamical variables used in atmospheric research can be found from basic introductory textbooks of meteorology (e.g. [1, 2]). Nevertheless, they are not commonly used in other fields and hence the relevant variables are first introduced. General conservation equations lay the foundations for all the atmospheric models so they are briefly discussed before describing the models. MLM is discussed in detail but only a short description of the mesoscale model MM5 is given because it is not the fundamental tool of this thesis and consequently, a detailed description is not necessary.

2.1 Main thermodynamical variables

2.1.1 Specific humidity

Water has a significant influence on the dynamics of the atmosphere. Water vapour is less dense than dry air and thus moist unsaturated air is more buoyant than dry air of the same temperature. In addition, temperature and moisture can interact between them through latent heat of phase changes. Water content of air is commonly described by the total specific humidity, q_t, which is defined as the mass fraction of total amount of water in a parcel of air:

$$q_t = \frac{m_{\mathrm{w}}}{m} \,. \tag{2.1}$$

Here the mass of water inside the parcel is $m_{\mathrm{w}} = m_{\mathrm{g}} + m_{\mathrm{l}} + m_{\mathrm{s}}$ where $m_{\mathrm{g}}, m_{\mathrm{l}}, m_{\mathrm{s}}$ are respectively the masses of gas, liquid and solid phases. Total mass of the parcel is $m = m_{\mathrm{d}} + m_{\mathrm{w}}$ where m_{d} is the mass of dry air. Water in solid and liquid phases are not considered in the MLM simulations of this thesis so they are left out in the following discussion.

2.1.2 Virtual temperature

Buoyancy is a significant driving force for turbulence in the CBL and therefore the effect of water on the density has to be considered in meteorological modeling. Density of a moist air parcel of volume V reads

$$\rho = \frac{m_{\mathrm{d}} + m_{\mathrm{v}}}{V} \,. \tag{2.2}$$

Density of dry air can hence be written as

$$\rho_{\mathrm{d}} = \rho \frac{m_{\mathrm{d}}}{m_{\mathrm{d}} + m_{\mathrm{v}}} = \rho(1 - q_{\mathrm{v}}) \,, \tag{2.3}$$

where q_{v} is the mass fraction of water vapour. Air in atmosphere can be adequately described by the ideal gas law. Dalton's law states that a mixture consisting of i constituents having partial pressures p_i has a total pressure of $p = \sum_i p_i$. By applying Dalton's law the ideal gas law for moist air can be written as

$$p = \rho R_{\mathrm{m}} T = \rho[(1 - q_{\mathrm{v}}) R_{\mathrm{d}} T + q_{\mathrm{v}} R_{\mathrm{v}} T] \,, \tag{2.4}$$

where gas constants of dry air and water vapour are $R_{\mathrm{d}} = 287.0\,\mathrm{J\,K^{-1}\,kg^{-1}}$ and $R_{\mathrm{v}} = 461.51\,\mathrm{J\,K^{-1}\,kg^{-1}}$ respectively [2]. The gas constant of the mixture is then given by

$$R_{\mathrm{m}} = (1 - q_{\mathrm{v}}) R_{\mathrm{d}} + q_{\mathrm{v}} R_{\mathrm{v}} \,, \tag{2.5}$$

which depends on the water content of air. This dependence is typically shifted to temperature by defining a virtual temperature, T_{v}, through the ideal gas law

$$p = \rho R_{\mathrm{d}} T_{\mathrm{v}} \,. \tag{2.6}$$

Virtual temperature is then the temperature required in a dry atmosphere to have the same density as in a moist atmosphere with the same pressure. Expression for virtual temperature is obtained from equations (2.4) and (2.6), giving

$$T_{\mathrm{v}} = T \left[1 + q_{\mathrm{v}} \left(\frac{R_{\mathrm{v}}}{R_{\mathrm{d}}} - 1 \right) \right] \,. \tag{2.7}$$

This is usually written in the following form:

$$T_{\mathrm{v}} \cong T(1 + 0.61 q_{\mathrm{v}}) \,. \tag{2.8}$$

For moist air, virtual temperature is always larger than the absolute temperature. It is thus one way to illustrate that moist air is indeed less dense than dry air.

2.1.3 Potential temperature

Potential temperature, θ, is the temperature that an air parcel would have if it would be adiabatically displaced from its current temperature and pressure to a standard pressure, p_0, generally taken as 10^5Pa. To derive an equation for potential temperature the first law of thermodynamics for ideal gas is written as

$$\mathrm{d}Q = c_p \mathrm{d}T - \alpha \mathrm{d}p \,, \tag{2.9}$$

where Q is specific thermal energy, $\alpha = \rho^{-1}$ is specific volume and $c_p = 1004\,\mathrm{J\,K^{-1}\,kg^{-1}}$ [2] is specific heat at constant pressure. Dividing equation (2.9) by temperature and employing ideal gas law gives the change in entropy in the following form:

$$\mathrm{d}s = \frac{\mathrm{d}Q}{T} = c_p \frac{\mathrm{d}T}{T} - R_{\mathrm{d}} \frac{\mathrm{d}p}{p} \,. \tag{2.10}$$

For adiabatic processes ($\mathrm{d}Q = 0$) the change in entropy is zero so equation (2.10) reduces to

$$\frac{c_p}{R_{\mathrm{d}}} \frac{\mathrm{d}T}{T} = \frac{\mathrm{d}p}{p} \,. \tag{2.11}$$

Integrating (2.11) from p_0 to p and using the definition of potential temperature $[T(p = p_0) = \theta]$ leads to

$$\frac{c_p}{R_\mathrm{d}} \ln \frac{T}{\theta} = \frac{p}{p_0} \,. \tag{2.12}$$

Finally, taking the antilog of both sides of equation (2.12) and rearranging the terms, the expressions for potential temperature reads:

$$\theta = T \left(\frac{p_0}{p} \right)^{\frac{R_\mathrm{d}}{c_p}} \,. \tag{2.13}$$

Potential temperature is also closely related to the stability of the atmosphere. Atmosphere with height independent potential temperature is called neutral or neutrally stable since it does not damp or amplify fluctuations of temperature or density. Neutral atmospheric conditions are typically encountered in the ML during the day and in the residual layer during the night. Air is said to be stable when potential temperature increases with height since in this case atmosphere tends to damp fluctuations. Stable air occur in the nocturnal ABL, in the FA and in the inversion layer. Potential temperature decreases with height in an unstable atmosphere where atmospheric fluctuations are amplified. Unstable air is found in the surface layer during the day time.

2.1.4 Virtual potential temperature

Virtual potential temperature is analogous to potential temperature but it takes moisture into account. The definition of virtual potential temperature is

$$\theta_\mathrm{v} = T_\mathrm{v} \left(\frac{p_0}{p} \right)^{\frac{R_\mathrm{d}}{c_p}} \,. \tag{2.14}$$

By using equations (2.8) and (2.13) this can be written as

$$\theta_\mathrm{v} \cong \theta(1 + 0.61 q_\mathrm{v}) \,. \tag{2.15}$$

Virtual potential temperature is conserved in adiabatic and isentropic processes. Therefore it removes adiabatic temperature variations due to changes in pressure during vertical motion of an air parcel. Furthermore, it can be shown that for small density and virtual temperature fluctuations the following relation holds [1]:

$$\frac{\rho'}{\overline{\rho}} = -\frac{{\theta_\mathrm{v}}'}{\overline{\theta}_\mathrm{v}} \,, \tag{2.16}$$

where the mean value of variable $\varphi \in \{\rho, \theta_\mathrm{v}\}$ is denoted by $\overline{\varphi}$ and the fluctuation from the mean is φ'. This result shows that the fluctuations in density (buoyancy) can described with virtual temperature fluctuations. This is advantageous since fluctuations in temperature are much easier to measure than fluctuations in density.

2.2 Governing equations

Governing equations for ABL dynamics are based on a set of conservation principles. These principles are conservation of mass, momentum, heat, moisture and other scalars, such as CO_2. The corresponding conservation equations are shortly introduced in this section.

2.2.1 Conservation of mass

Conservation of mass, or continuity equation reads

$$\frac{\partial \rho}{\partial t} = -\frac{\partial \rho u_j}{\partial x_j} \,. \tag{2.17}$$

Here x_j represent the Cartesian coordinates, $\mathbf{x} = (x, y, z)$, and u_j is the component of wind velocity, $\mathbf{u} = (u, v, w)$, in the x_j direction. Summation over index j is assumed in this equation. Incompressibility assumption can be applied for shallow ABLs [39, 40] which reduces equation (2.17) to

$$\frac{\partial u_j}{\partial x_j} = 0 \,. \tag{2.18}$$

2.2.2 Conservation of momentum

The conservation of momentum is expressed by the Navier-Stokes equation of motion

$$\frac{\partial u_i}{\partial t} = -u_j \frac{\partial u_i}{\partial x_j} - \frac{1}{\rho}\frac{\partial p}{\partial x_i} - g\delta_{i3} - 2\epsilon_{ijk}\Omega_j u_k + \frac{1}{\rho}\frac{\partial \tau_{ij}}{\partial x_j} \,, \tag{2.19}$$

where summation over index j is again assumed. The first term on the right hand side (RHS) of equation (2.19) describes advection and the second describes forces due to pressure gradients. Third term on the RHS is the vertical acceleration due to gravity, where g denotes the acceleration of gravity and δ_{ij} is the Kronecker delta symbol. Fourth term on the RHS of equation (2.19) is the Coriolis force due to Earth's rotation. The angular velocity vector of Earth's rotation is denoted by ω so the components of the angular velocity vector Ω_j are $(0, \omega\cos\lambda, \omega\sin\lambda)$, where λ is the latitude. Furthermore, ϵ_{ijk} is the Levi-Civita symbol. Influence of viscous stress is represented by the last term on the RHS of equation (2.19), where τ_{ij} is the shear stress tensor. Besides the surface layer, the last term is several orders of magnitude smaller than the other terms and can be neglected [1]. Momentum equation (2.19) is not exploited in the MLM used in this work but it was introduced here for completeness and since the mesoscale model MM5 uses a simplified version of this equation.

2.2.3 Conservation of scalars

Conservation equation for heat, moisture and other scalars reads

$$\frac{\partial \varphi}{\partial t} = -\frac{\partial u_j \varphi}{\partial x_j} + S_\varphi \,, \tag{2.20}$$

where S_φ includes the sources and sinks of scalar φ. Heat conservation is typically written for potential temperature, θ and moisture conservation for total specific humidity, q_t. Sources and sinks for heat and moisture include for example phase changes, chemical reactions, convergence and divergence of net radiation flux and dissipation of kinetic energy by molecular motions. CO_2 is a passive non-reactive scalar so there are no sources or sinks of CO_2 in the atmosphere. In the case of MLM the source/sink term can however contain also large scale advection, as will be discussed in the next section.

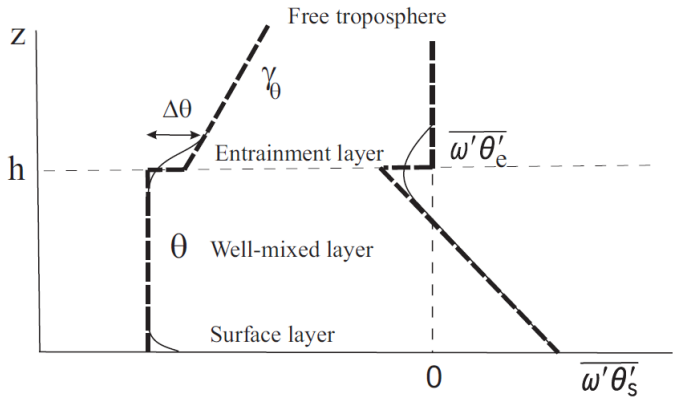

Figure 2.1: Schematic vertical profiles of potential temperature and its turbulent flux in a realistic case (thin solid line) and in MLM (thick dashed line) [49].

2.3 Mixed-layer model

The MLM used in this thesis is a one-dimensional slab model [33–37]. It assumes vertically constant bulk values of conservative mean variables in the CBL and an infinitesimally thin entrainment zone and surface layer compared to the CBL depth. On the basis of the these assumptions a realistic vertical profile of potential temperature and its turbulent flux can be approximated with highly simplified profiles as shown in Figure 2.1. Vertical profiles of other conserved mean variables can be approximated in a similar way. MLM based on the profile shown in Figure 2.1 is called a zeroth-order (jump) model due to the zeroth-order discontinuity at the ML top. First-order MLMs are also used to study the ABLs [41–43] but they are not considered in this thesis. In the case of zeroth-order MLM, a relatively simple set of ML equations can be written for the temporal evolution of potential temperature, moisture and CBL depth. Models based on these ML assumptions have been widely used to describe BLs both in the atmosphere (e.g. [34–37]) and in the ocean (e.g. [44–47]). Oceanic and atmospheric MLMs differ mainly by the equation of state [48]. In this section the ML equations and parametrization used in this thesis are described.

2.3.1 Mixed-layer equations

ML equations are derived by starting from the general scalar conservation equation (2.20). First, horizontal homogeneity is assumed over the studied region. Second, φ is decomposed into its mean $\overline{\varphi}$ and fluctuation φ' by using so called Reynolds decomposition:

$$\varphi = \overline{\varphi} + \varphi' \,. \tag{2.21}$$

Here average $\overline{\varphi}$ should represent a horizontal average but by Taylor's hypothesis [50] it can also be a time average if the measurements are taken at a fixed point. By introducing Reynolds decomposition in equation (2.20), the equation

for the mean variables reads:

$$\frac{\partial \overline{\varphi}}{\partial t} = -\frac{\partial \overline{u_j \varphi}}{\partial x_j} + \overline{S_\varphi}\,. \tag{2.22}$$

The rules of Reynolds decomposition allows equation (2.22) to be written as (see for example [1])

$$\frac{\partial \overline{\varphi}}{\partial t} = -\frac{\partial \overline{u_j \varphi}}{\partial x_j} - \frac{\partial \overline{u_j' \varphi'}}{\partial x_j} + \overline{S_\varphi}\,, \tag{2.23}$$

where quantity $\partial \overline{u_j' \varphi'}/\partial x_j$ describes the divergence of turbulent fluxes. In convective conditions the divergence of horizontal turbulent fluxes can be neglected at least if the spatial scale of horizontal flux divergence is much larger than the CBL depth [51, 52]. By using the chain rule of differentiation the first term on the RHS can be written as

$$\frac{\partial \overline{u_j \varphi}}{\partial x_j} = \overline{u_j}\frac{\partial \overline{\varphi}}{\partial x_j} + \overline{\varphi}\frac{\partial \overline{u_j}}{\partial x_j}\,. \tag{2.24}$$

The second term on the RHS is zero by the conservation of mass (equation 2.18) and the horizontal gradients of φ are zero due to the assumed horizontal homogeneity. Therefore, equation (2.23) reduces to

$$\frac{\partial \overline{\varphi}}{\partial t} = -\overline{w}\frac{\partial \overline{\varphi}}{\partial z} - \frac{\partial \overline{w' \varphi'}}{\partial z} + \overline{S_\varphi}\,. \tag{2.25}$$

Notice that even though horizontal advection terms were neglected the contribution of large scale advection can be included in $\overline{S_\varphi}$. Advective contributions from spatial scales smaller than the horizontal extent of the ML averaging are however filtered out in this process.

Conserved variables are usually well-mixed by turbulence in a CBL. It is hence assumed that these variables can be well represented in the entire CBL by a single bulk value known as a ML value. This ML value is defined as

$$\varphi(t)_{\mathrm{ml}} = \frac{1}{h}\int_{z_0}^{h} \overline{\varphi}(t, z)\,\mathrm{d}z\,, \tag{2.26}$$

where h is the depth of the CBL and z_0 is a surface roughness length. Several definitions have been proposed for the CBL depth [53]. One common way is to define it as the height where the most negative heat flux occurs [1]. The assumption made above is called ML assumption and the model get its name from it.

Next, equation (2.25) is integrated over the CBL depth and the definition of the ML value is used to give:

$$\frac{\partial \varphi_{\mathrm{ml}}}{\partial t} = \frac{\overline{w'\varphi'}|_{\mathrm{s}} - \overline{w'\varphi'}|_{\mathrm{e}}}{h} + \int_{z_0}^{h} \overline{S_\varphi}\,\mathrm{d}z\,, \tag{2.27}$$

where $\overline{w'\varphi'}|_{\mathrm{s}}$ is the flux of φ at the surface and $\overline{w'\varphi'}|_{\mathrm{e}}$ is the corresponding flux at the top of the ML. The last term on the RHS of equation (2.27) includes sources and sinks of φ. Large scale horizontal advection of φ is introduced in

this term and its ML value is denoted by A_φ. Other sources/sinks, like radiation divergence and phase changes of water are not considered in this work. Equation (2.27) is the ML conservation equation for mean bulk values of potential temperature, moisture and other scalars.

Turbulent flux at top of the CBL is due to exchange of air masses between the CBL and the FA. This turbulent flux, called entrainment flux, depends on the growth of the CBL and is written in the ML theory as [33, 54]:

$$\overline{w'\varphi'}|_e = -\Delta\varphi \left(\frac{\partial h}{\partial t} - w_\mathrm{s} \right) = -\Delta\varphi w_\mathrm{e} \,, \tag{2.28}$$

where $\Delta\varphi = \varphi^\mathrm{FA} - \varphi_\mathrm{ml}$ is the difference between φ_ml and $\overline{\varphi}$ in the FA just above the inversion, denoted by φ^FA. The entrainment velocity w_e is defined as $w_\mathrm{e} = \partial h/\partial t - w_\mathrm{s}$, where w_s is the large scale mean vertical wind velocity, also called subsidence. Subsidence, w_s, can be calculated from the large scale divergence, ω_s, as

$$w_\mathrm{s} = -\omega_\mathrm{s}\, h \tag{2.29}$$

which is valid in the special case of constant divergence with height [1].

MLM assumes that $\overline{\varphi}$ is linear with height in the FA. Furthermore, advection is considered as the only source/sink of φ in the FA. Consequently, the temporal evolution of $\Delta\varphi$ reads:

$$\frac{\partial \Delta\varphi}{\partial t} = \gamma_\varphi \left(\frac{\partial h}{\partial t} - w_\mathrm{s} \right) + A_\varphi^\mathrm{FA} - \frac{\partial \varphi_\mathrm{ml}}{\partial t} \,, \tag{2.30}$$

in which γ_φ is the vertical gradient of $\overline{\varphi}$ in the FA and A_φ^FA is advection in the FA. This advection in the FA is sometimes neglected even when advection in the ML is included in the model [55, 56].

The set of ML equations includes equations (2.27), (2.28) and (2.30) for prognostic variables φ_ml, $\Delta\varphi$ and h. Subsidence w_s, FA lapse rate γ_φ and advection in the CBL A_φ and in the FA A_φ^FA are related to large scale atmospheric conditions and they are prescribed in the MLM. Moreover, surface turbulent flux $\overline{w'\varphi'}|_\mathrm{s}$ is usually prescribed based on the field measurements. Entrainment flux $\overline{w'\varphi'}|_\mathrm{e}$ is however difficult to measure and therefore it has to be parametrized to close the set of ML equations.

2.3.2 Parametrization of entrainment fluxes

There exists many different parametrizations of the entrainment fluxes [36, 37, 54, 57–61]. For the case of free convection, the buoyancy flux at the top of the ML is nearly a constant fraction of the surface buoyancy flux [54, 62]:

$$\overline{w'\theta_\mathrm{v}'}|_\mathrm{e} = \beta_{\theta_\mathrm{v}} \overline{w'\theta_\mathrm{v}'}|_\mathrm{s} \,. \tag{2.31}$$

This simple but commonly used parametrization is included in the MLM considered in this thesis. This parametrization also assumes that the changes in the surface flux are immediately felt at top of the ML. In practice, a typical time for air to circulate between the surface and the ML top, called convective time scale, is about 10-20 minutes [1]. Parametrization given by equation (2.31) does not include wind velocity so the effect of the shear driven turbulence is not explicitly taken into account in this parametrization scheme.

Buoyancy flux can be written in terms of potential temperature and fluxes of temperature and moisture by making use of equation (2.15):

$$\overline{w'\theta'_{\mathrm{v}}} \approx \overline{w'\theta'} + 0.61(\overline{\theta}\,\overline{w'q'_{\mathrm{v}}})\,, \tag{2.32}$$

where terms $\overline{q_{\mathrm{v}}}\,\overline{w'\theta'}$ and $\overline{w'\theta'q'_{\mathrm{v}}}$ are neglected since they are much smaller than the other terms. Finally, CBL growth can be solved by writing equation (2.28) for virtual potential temperature as

$$\overline{w'\theta'_{\mathrm{v}}} = \left(\frac{\partial h}{\partial t} - w_{\mathrm{s}}\right)\Delta\theta_{\mathrm{v}} \tag{2.33}$$

where the virtual potential temperature difference $\Delta\theta_{\mathrm{v}}$ across the inversion layer is given by

$$\Delta\theta_{\mathrm{v}} = \Delta\theta + 0.61(q_{\mathrm{v,ml}}\Delta\theta + \theta_{\mathrm{ml}}\Delta q_{\mathrm{v,ml}} + \Delta\theta\Delta q_{\mathrm{v,ml}})\,. \tag{2.34}$$

This closes the set of ML equations and completes the framework of the MLM used in this thesis. Explicit form for temporal evolution of CBL depth is not obtained from these equations and therefore the equations are solved numerically. Complete set of ML equations included in the MLM employed in this thesis can be found from Appendix A.

2.4 Mesoscale model MM5

The fifth-generation Pennsylvania State University - National Center of Atmospheric Research Mesoscale Model (MM5) [38] is a numerical atmospheric model used for simulating and predicting mesoscale and regional scale atmospheric circulation. In meteorology, mesoscale can be defined as those atmospheric systems with horizontal extent large enough for hydrostatic approximation to be applicable to the vertical pressure distribution but yet small enough for both ageostrophic advection and Coriolis accelerations to be important [63, 64]. Practically this implies horizontal scales from few kilometers to several hundreds of kilometers and vertical scales from tens of meters to the depth of the troposhere [64].

MM5 model uses terrain influenced vertical coordinates and the current version contains a capability for both nonhydrostatic and hydrostatic simulations. Nonhydrostatic dynamics enables the model to be used at a few-kilometer scale. Furthermore, MM5 allows multiple nesting with nested domains running at the same time and completely interacting. MM5 includes many schemes for physical parametrizations. The parametrization schemes used in this thesis were Kain-Fritsch scheme for cumulus parametrization [65], Simple Ice for explicit moisture schemes [38] and Medium Range Forecast scheme for the BL [66]. Simulations require initial conditions and lateral boundary conditions updated every six hours from analysis of the European Center for Medium-Range Weather Forecasts (ECMWF), which consists of gridded meteorogical data over the whole time period of the simulation. This data is interpolated in MM5 to its computational grid. MM5 itself does not contain an option to simulate atmospheric CO_2 concentrations but it have been coupled to other models to include CO_2 [67, 68]. Coupled models were however not used in this thesis so CO_2 mixing ratio information could not be obtained from the mesoscale simulations.

Chapter 3

Sensitivity analysis

3.1 CO_2 mixing ratio sensitivities

The following derivation of the sensitivity of CO_2 mixing ratio to errors in the CBL variables follows closely the derivation by Pino *et al.* [32]. Their notation is also followed so subscript ml is left out from the ML values. Substituting equation (2.28) into (2.27) and neglecting the large scale subsidence, the conservation equation for the CO_2 mixing ratio reads:

$$\frac{\partial C}{\partial t} = \frac{\overline{w'c'}|_{\mathrm{s}}}{h} + \frac{\Delta C}{h}\frac{\partial h}{\partial t} + A_c\,, \tag{3.1}$$

where C denotes the CO_2 mixing ratio and A_c is the advection rate of CO_2 in the ML which is treated as constant in time. Multiplying equation (3.1) by h and using the definition of ΔC leads to

$$\frac{\partial}{\partial t}(Ch) = \overline{w'c'}|_s + C^{\mathrm{FA}}\frac{\partial(h-h_0)}{\partial t} + A_c h\,, \tag{3.2}$$

where h_0 is the initial CBL depth. In the MLM the CO_2 mixing ratio just above the inversion is given by

$$C^{\mathrm{FA}} = C_0^{\mathrm{FA}} + \gamma_c(h-h_0) + \int_{t_0}^{t} A_c^{\mathrm{FA}}\,\mathrm{d}\tilde{t}\,, \tag{3.3}$$

where C_0^{FA} is the initial CO_2 mixing ratio above the inversion and A_c^{FA} is the advection rate of CO_2 in the FA. Vertical gradient of CO_2 mixing ratio in the FA, γ_c, and advection in the FA, A_c^{FA}, are considered constant during the day. Substituting (3.3) into (3.2) and integrating on time from t_0 to t leads to

$$\begin{aligned} Ch - C_0h_0 = {} & \int_{t_0}^{t} \overline{w'c'}|_{\mathrm{s}}\,\mathrm{d}\tilde{t} + \frac{\gamma_c}{2}(h-h_0)^2 + (A_c - A_c^{\mathrm{FA}})\int_{t_0}^{t} h\,\mathrm{d}\tilde{t} + \\ & + \left[C_0^{\mathrm{FA}} + (t-t_0)A_c^{\mathrm{FA}}\right](h-h_0)\,. \end{aligned} \tag{3.4}$$

Therefore, the expression for the time evolution of the CO_2 mixing ratio reads:

$$\begin{aligned} C = {} & C_0\frac{h_0}{h} + \frac{\gamma_c}{2h}(h-h_0)^2 + \frac{t-t_0}{h}\langle\overline{w'c'}\rangle_{\mathrm{s}} + \frac{A_c - A_c^{\mathrm{FA}}}{h}\int_{t_0}^{t} h\,\mathrm{d}\tilde{t} + \\ & + \left[C_0^{\mathrm{FA}} + (t-t_0)A_c^{\mathrm{FA}}\right]\left(1 - \frac{h_0}{h}\right)\,, \end{aligned} \tag{3.5}$$

where $\langle\overline{w'c'}\rangle_{\mathrm{s}} = \left[\int_{t_0}^{t} \overline{w'c'}|_{\mathrm{s}}\,\mathrm{d}\tilde{t}\right]/(t-t_0)$ is the time averaged CO_2 surface flux. The fourth term on the RHS of equation (3.5) is proportional to the time integral of the CBL depth and therefore the CO_2 mixing ratio depends on the history of the CBL depth evolution if advection in the CBL and in the FA do not have the same value.

Sensitivities of CO_2 mixing ratio to errors in the CBL variables are obtained by taking partial derivatives of C with respect to the corresponding variables. This yields to the following sensitivity expressions:

$$\frac{\partial C}{\partial C_0} = \frac{h_0}{h}\,, \tag{3.6}$$

$$\frac{\partial C}{\partial C_0^{\mathrm{FA}}} = 1 - \frac{h_0}{h}\,, \tag{3.7}$$

$$\frac{\partial C}{\partial \gamma_c} = \frac{(h-h_0)^2}{2\,h}\,, \tag{3.8}$$

$$\frac{\partial C}{\partial \langle\overline{w'c'}\rangle_{\mathrm{s}}} = \frac{t-t_0}{h}\,, \tag{3.9}$$

$$\frac{\partial C}{\partial h_0} = -\gamma_c + \frac{1}{h}\left[\gamma_c\,h_0 + C_0 - C_0^{\mathrm{FA}} - (t-t_0)A_c^{\mathrm{FA}}\right]\,, \tag{3.10}$$

$$\frac{\partial C}{\partial A_c} = \frac{1}{h}\int_{t_0}^{t} h\,\mathrm{d}\tilde{t}\,, \tag{3.11}$$

$$\frac{\partial C}{\partial A_c^{\mathrm{FA}}} = (t-t_0) - \frac{1}{h}\int_{t_0}^{t} h\,\mathrm{d}\tilde{t}\,, \tag{3.12}$$

$$\begin{aligned}\frac{\partial C}{\partial h} = {} & \frac{1}{h^2}\left\{h_0\left[C_0^{\mathrm{FA}} + (t-t_0)A_0^{\mathrm{FA}} - C_0\right] - \frac{\gamma_c\,h_0^2}{2} - (t-t_0)\langle\overline{w'c'}\rangle_{\mathrm{s}}\right\} \\ & - \frac{1}{h^2}\left\{(A_c - A_c^{\mathrm{FA}})\int_{t_0}^{t} h\,\mathrm{d}\tilde{t}\right\} + \frac{\gamma_c}{2}\,.\end{aligned} \tag{3.13}$$

The last four sensitivities are affected by the CO_2 advection and the last three sensitivities depend on the history of the CBL depth. Equations (3.6)-(3.13) are used in Section 5 to estimate the relative effect of errors in different CBL variables on the uncertainties in the CO_2 mixing ratio. Assuming that the errors are small, the sensitivities are linearly related to the error in the CO_2 mixing ratio, δC, through the following relation [69]:

$$\delta C = \sum_{\phi}\left|\frac{\partial C}{\partial \phi}\right|\cdot|\delta\phi|\,, \tag{3.14}$$

where ϕ denotes the different variables influencing the evolution of C. However, the error in the CO_2 mixing ratio due to incorrect CBL depth evolution cannot be correctly estimated from equation (3.14). This is because CO_2 mixing ratio depends on the history of the CBL depth and consequently, its errors depend also on the past errors.

Equation (3.14) also assumes that $h(t)$ and h_0 are independent since their dependence is not taken into account. In practice, an error in h_0 can propagate to $h(t)$ depending on the situation. For example, if h_0 is obtained from a radio sounding measurement done in the morning and the subsequent evolution of h is

simulated, then the error in h_0 propagates to $h(t)$. In this case the dependence $\partial h/\partial h_0$ should also be considered in the error estimation. This dependence can be obtained from the ML equations and it is derived in Appendix B. However, if h is measured also at later time when C is evaluated, the errors in h_0 and $h(t)$ can be completely independent. For simplicity, the latter case is assumed in the above equations and in the following analysis.

Another assumption made in the above equations is the time and height independence of A_c and A_c^{FA}. In reality, having an approximately constant advection during the whole day is rather an exception than a rule. In fact, this would require that the product of large scale horizontal wind and horizontal gradient of C would remain constant during the day. In this work, time and height independent advection is however used for simplicity. Height and time independence of γ_c is also an approximation which is not generally true. In the absence of advection in the FA the time independence of γ_c can be justified on diurnal time scales since changes in the FA CO_2 mixing ratio through other processes than advection are usually much slower than the changes occurring in the ML concentration. However, even if the FA concentration profile does not change with time it does not have to be exactly linear with height and hence γ_c could also depend on height. Constant γ_c has been successfully used in MLM simulations [26] and often it is reasonably good and justified approximation.

3.2 Inferred CO_2 surface flux sensitivities

The sensitivity analysis presented in the previous section for the CO_2 mixing ratio is also conducted for the inferred CO_2 surface flux. The CO_2 surface flux solved from equation (3.4) reads

$$\langle\overline{w'c'}\rangle_{\mathrm{s}} = \frac{1}{t-t_0}\left[Ch - C_0h_0 - C_0^{\mathrm{FA}}(h-h_0) - \frac{\gamma_c}{2}(h-h_0)^2 + (A_c^{\mathrm{FA}} - A_c)\int_{t_0}^{t} h\,\mathrm{d}\tilde{t}\right] - A_c^{\mathrm{FA}}(h-h_0)\,. \tag{3.15}$$

By taking the partial derivatives of this equation with respect to different CBL variables the following sensitivity equations are obtained:

$$\frac{\partial\langle\overline{w'c'}\rangle_{\mathrm{s}}}{\partial C_0} = \frac{-h_0}{t-t_0}\,, \tag{3.16}$$

$$\frac{\partial\langle\overline{w'c'}\rangle_{\mathrm{s}}}{\partial C_0^{\mathrm{FA}}} = \frac{h_0 - h}{t - t_0}\,, \tag{3.17}$$

$$\frac{\partial\langle\overline{w'c'}\rangle_{\mathrm{s}}}{\partial \gamma_c} = -\frac{(h - h_0)^2}{2\,(t - t_0)}\,, \tag{3.18}$$

$$\frac{\partial\langle\overline{w'c'}\rangle_{\mathrm{s}}}{\partial C} = \frac{h}{t - t_0}\,, \tag{3.19}$$

$$\frac{\partial\langle\overline{w'c'}\rangle_{\mathrm{s}}}{\partial h_0} = \frac{1}{t - t_0}\left[C_0^{\mathrm{FA}} - C_0 + \gamma_c(h - h_0)\right] + A_c^{\mathrm{FA}}\,, \tag{3.20}$$

$$\frac{\partial\langle\overline{w'c'}\rangle_{\mathrm{s}}}{\partial A_c} = -\frac{1}{t - t_0}\int_{t_0}^{t} h\,\mathrm{d}\tilde{t}\,, \tag{3.21}$$

$$\frac{\partial\langle\overline{w'c'}\rangle_{\mathrm{s}}}{\partial A_c^{\mathrm{FA}}} = \frac{1}{t - t_0}\int_{t_0}^{t} h\,\mathrm{d}\tilde{t} - (h - h_0)\,, \tag{3.22}$$

$$\frac{\partial\langle\overline{w'c'}\rangle_{\mathrm{s}}}{\partial h} = \frac{1}{t - t_0}\left[C - C_0^{\mathrm{FA}} - \gamma_c(h - h_0)\right] - A_c^{\mathrm{FA}}\,. \tag{3.23}$$

Once again, the CO_2 advection only contributes to the last four sensitivities. Besides the assumptions and approximations considered before, here it is additionally assumed that C is directly measured at different times and so the errors in C do not depend on the other variables.

Chapter 4

Observations

4.1 Measurement site

The observational data used in this thesis was recorded at the Cabauw meteorological tower located in the Netherlands (51°58′N, 4°56′E). The immediate surroundings of the tower are flat and covered with short grass extending for several hundreds of meters. This surrounding region have been extensively described in previous research [70, 71]. Further surroundings consists of meadows and fields with scattered villages, orchards and lines of trees. This region is also rather flat with a surface elevation of only few meters within a distance of at least 20 km [72]. River Lek is situated 1 km South-East and the North Sea approximately 50 km West of the Cabauw site. Wind flow is unperturbed over an upstream distance of about 2 km in the predominant wind direction (southwest) at the site [71].

4.2 Meteorological measurements

Measurement sensors for wind, temperature, humidity and carbon dioxide are placed at several heights at the Cabauw 213 m tower. Temperature sensors are placed at 2, 10, 20, 30, 80, 140 and 200 m, whereas CO_2 mixing ratio is measured at 20, 60, 120 and 200 m. Carbon dioxide mixing ratios were measured with a Siemens Ultramat 5 NDIR with a resolution of 0.1 ppm [73]. Turbulent fluxes of momentum, sensible heat, latent heat and CO_2 are also recorded along the tower at 5, 60, 100 and 180 m. Carbon dioxide flux was measured at 10 Hz with an IFM open-path gas analyzer [74] at 5 m level and with a LI-COR LI 7500 open-path infrared gas analyzer at the three higher levels. Eddy covariances are computed on 30 minute basis by substracting the mean values of vertical wind, temperature and CO_2 from the measured time series. More detailed description of the flux measurements is given by Werner *et al.* [72], Bosveld *et al.* [75] and Vermeulen *et al.* [73]. Same days were also analyzed by Casso *et al.* [28] and they already performed some analysis regarding the errors of the flux measurements. CBL depth was determined from the wind profiler measurements. Radio sounding measurements took place twice a day at the synoptical station de Bilt located about 25 km from Cabauw.

Chapter 5

Results

5.1 25$^{\text{th}}$ September 2003

The first analyzed day is 25$^{\text{th}}$ September 2003. This is a well characterized convective day with clear skies and constant winds of 4-5 m s^{-1} during the day. Advection of heat, moisture and CO_2 are nearly absent during the day. The previous night was characterized by a shallow and stably stratified ABL [28].

MLM simulation and the sensitivity analysis have been previously done for this day by Pino *et al.* [32]. However, advection was not considered in their study since its contribution to the CO_2 budget was small on this day [28]. To complete the analysis of this day the ML experiments conducted by Pino *et al.* are here reproduced with CO_2 advection included in the MLM. Furthermore, the effect of CO_2 conditions on the sensitivities is considered and the influence of subsidence on the CO_2 mixing ratio uncertainties is demonstrated.

5.1.1 Mixed-layer simulation

Initial values and temporal evolution of the surface fluxes prescribed for the MLM simulation are presented in Table 5.1. Apart from the CO_2 advection, these values are prescribed following Pino *et al.* who based the choice of the values on the observations taken at the Cabauw measurement site [32]. The MLM simulations run from 6 to 18 in Coordinated Universal Time (UTC) which was the period of positive latent heat fluxes. The diurnal evolution of CBL depth, potential temperature and CO_2 mixing ratio obtained from the MLM simulation are presented in Figure 5.1 together with the observations taken along the meteorological tower. Because no land surface model was considered, the CO_2 advection has no effect on the other CBL variables except the CO_2 mixing ratio and therefore the evolution of CBL depth and potential temperature are exactly the same as obtained by Pino *et al.* and the evolution of these variables compares satisfactory with the observations.

The CO_2 mixing ratio evolution shown in Figure 5.1c instead deviates from the observations and from the non-advective MLM simulation because of the prescribed CO_2 advection in the ML. This deviation increases towards the end of the simulation since CO_2 is continuously advected to the ML. During the fast growth of the ML this deviation temporarily decreases since CO_2 is diluted by the ML growth. CO_2 was advected in the ML but not in the FA (see Table 5.1)

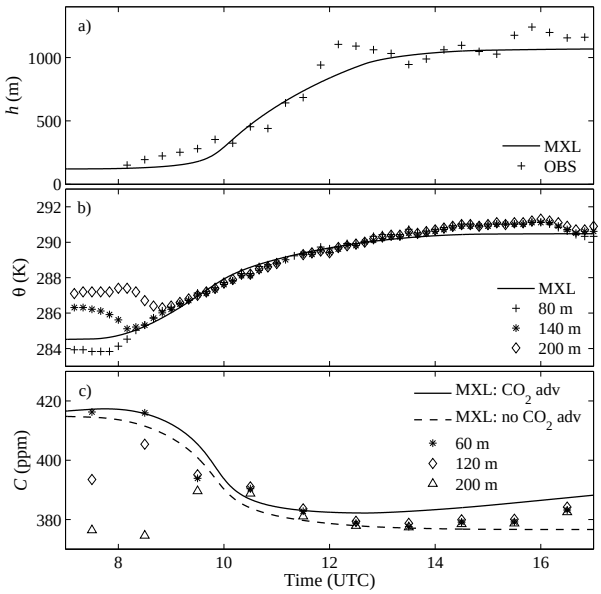

Figure 5.1: Observed (symbols) diurnal evolution of a) CBL depth obtained by wind profiler, b) potential temperature and c) CO_2 mixing ratio at different height of the Cabauw tower on 25$^{\text{th}}$ September 2003 together with the corresponding evolutions obtained from the MLM simulation with CO_2 advection (solid line). The CO_2 mixing ratio evolution obtained from the MLM simulation without CO_2 advection is also shown (dashed line). Initial and prescribed values of the MLM simulation are shown in Table 5.1.

because this case has a larger effect on the entrainment fluxes. Consequently, the non-trivial impact of advection on the CO2 mixing ratio evolution can be more easily recognized. This advection is deliberately set to be larger than the actual average advection on this day so that the contribution of advection can be seen more clearly in the following sensitivity analysis.

5.1.2 CO_2 mixing ratio uncertainties

Sensitivity of CO_2 mixing ratio to uncertainties associated to CBL dynamics or CO_2 characteristics is now evaluated from equations (3.6)-(3.11). Following Pino *et al.* [32] the change in the sensitivities with different atmospheric conditions is quantified by performing a set of MLM simulations where the initial inversion strength, $\Delta\theta_0$, and FA potential temperature lapse rate, γ_θ, are systematically changed. 41×41 MLM simulations are conducted ranging $\Delta\theta_0 \in [0.2, 5]\,(\mathrm{K})$ and $\gamma_\theta \in [10^{-3}, 10^{-2}]\,(\mathrm{K\,m^{-1}})$ respectively. In all these simulations potential temperature lapse rate and CO_2 surface flux are kept constant during the day. The other variables have the values shown in Table 5.1.

To ease the interpretation of the results, the influence of $\Delta\theta_0$ and γ_θ on the CBL evolution and on the CO_2 mixing ratio is first considered in five different

Table 5.1: Initial values and temporal evolution of the surface fluxes for the ML based on the observations taken at Cabauw (The Netherlands) on 25th September 2003. The other values besides A_c and A_c^{FA} are prescribed in the MLM following Pino *et al.* [32]. Time t is given in seconds and it ranges from zero to 43200 s.

Property	Value
CBL properties	
Initial CBL depth, h_0 (m)	120
Large scale subsidence velocity, w_{s} ($\mathrm{m\,s^{-1}}$)	0
Heat	
$\overline{w'\theta'}\vert_{\mathrm{s}}$ (07:30-15:00 UTC) ($\mathrm{K\,m\,s^{-1}}$)	$0.08\,\sin\left(\frac{\pi(t-5400)}{27000}\right)$
Entrainment to surface sensible flux ratio, $\beta_{\theta_{\mathrm{v}}}$	0.3
θ_0 (K)	284.5
$\Delta\theta_0$ (K)	3.5
γ_θ ($\mathrm{K\,m^{-1}}$)	
$h < 950$ m	$3.6{\cdot}10^{-3}$
$h > 950$ m	$15{\cdot}10^{-3}$
Moisture	
$\overline{w'q'}\vert_{\mathrm{s}}$, (06:00-18:00 UTC) ($\mathrm{g\,kg^{-1}\,m\,s^{-1}}$)	$0.087\,\sin\left(\frac{\pi t}{43200}\right)$
q_0 ($\mathrm{g\,kg^{-1}}$)	4.3
Δq_0 ($\mathrm{g\,kg^{-1}}$)	-0.8
γ_q ($\mathrm{g\,kg^{-1}\,m^{-1}}$)	$-1.5{\cdot}10^{-3}$
Carbon dioxide	
$\overline{w'c'}\vert_{\mathrm{s}}$, (08:00-15:30 UTC) ($\mathrm{ppm\,m\,s^{-1}}$)	$-0.1\,\sin\left(\frac{\pi(t-7200)}{27000}\right)$
C_0 (ppm)	415
ΔC_0 (ppm)	-40
γ_c ($\mathrm{ppm\,m^{-1}}$)	$-3{\cdot}10^{-3}$
A_c ($\mathrm{ppm\,s^{-1}}$)	$5{\cdot}10^{-4}$
A_c^{FA} ($\mathrm{ppm\,s^{-1}}$)	0

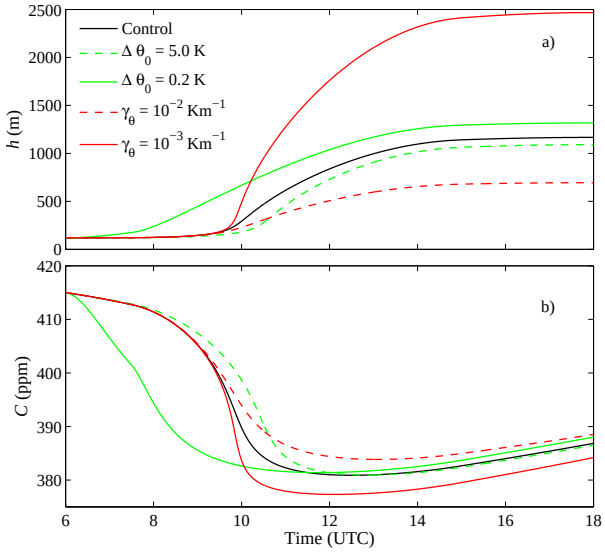

Figure 5.2: Time evolution of a) the CBL depth and b) the CO_2 mixing ratio obtained from the MLM simulations with different values of γ_θ and $\Delta\theta_0$. The control case has $\gamma_\theta = 3.6 \cdot 10^{-3}\,\mathrm{K\,m^{-1}}$, and $\Delta\theta_0 = 3.5\,\mathrm{K}$. In the figure legend, if the potential temperature lapse rate or inversion strength is not shown, the value for the control case applies.

cases. The first case is the advective case presented in Figure 5.1 before but with $\gamma_\theta = 0.0036\,\mathrm{K\,m^{-1}}$ and $\overline{w'c'}|_\mathrm{s} = -0.1\,\mathrm{ppm\,m\,s^{-1}}$ constant in time. From now on this case is referred as the control case. In the other four cases, the value of $\Delta\theta_0$ or γ_θ is changed from the control value to one of the extreme values used in the sensitivity analysis. The evolution of CBL depth and CO_2 mixing ratio for these five cases is presented in Figure 5.2. Initial inversion strength, $\Delta\theta_0$, essentially changes the time of the morning transition with large values delaying and small values advancing this transition. Morning transition is seen as a substantial increase in the growth rate of the CBL depth and consequently, this leads to a significant decrease in the CO_2 mixing ratio (See Figure 5.2b). Potential temperature lapse rate in the FA instead does not have much effect before the morning transition but it controls the growth rate of the CBL depth after the morning transition. Therefore, the final values of CBL depth and CO_2 mixing ratio are greatly determined by its value.

Following Pino *et al.* [32] and Jacobs and De Bruin [69], the sensitivity of CO_2 mixing ratio to variable ϕ is normalized as

$$RSC_\phi = \frac{\partial C}{\partial \phi} \cdot \frac{\phi}{C}\,, \tag{5.1}$$

where $\frac{\partial C}{\partial \phi}$ is obtained from expressions (3.6)-(3.11). The time evolution of relative sensitivities calculated from equation (5.1) are shown in Figure 5.3a for the control case. Relative sensitivity $RSC_{A_c^{\mathrm{FA}}}$ is not plotted since it is zero in the absence of advection in the FA. In general, the relative sensitivities do not

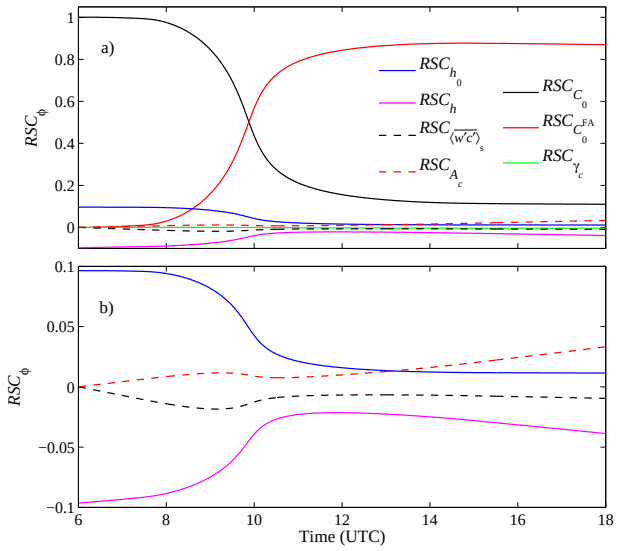

Figure 5.3: Time evolution of relative sensitivities of CO_2 mixing ratio to a) all the CBL variables except A_c^{FA} for the control and b) a detail of a). Relative sensitivity $RSC_{A_c^{\mathrm{FA}}}$ is not plotted since in this case it is zero during the whole day.

significantly differ from the non-advective case (not shown) [32]. All the relative sensitivities are however slightly changed since they depend on the CO_2 mixing ratio which is changed by advection. Relative sensitivities RSC_h and RSC_{A_c} change the most since the sensitivities $\partial C/\partial h$ and $\partial C/\partial A_c$ are modified by advection in the CBL.

Relative influence of advection on the CO_2 mixing ratio uncertainties is small during the whole day. It is however interesting to compare the importance of advection and CO_2 surface flux on the diurnal evolution of the CO_2 mixing ratio. Figure 5.3b shows a detail of Figure 5.3a so the evolution of these sensitivities can be seen more easily. According to this figure, the influence of CO_2 surface flux is slightly greater during the morning and during midday but advection becomes more important at the end of the day. Figure 5.3b however considers the control case where the CO_2 surface flux is prescribed as constant during the day. In reality, the surface flux is approximately sinusoidal and therefore advection is more important also during the morning. In general, advection can often be more important source or sink of CO_2 during the mornings and evenings when the CO_2 uptake due to vegetation is small. During the midday either one can dominate depending on the specific conditions.

To analyze the influence of CBL conditions on the sensitivity of CO_2 mixing ratio to advection, the time evolution of $\partial C/\partial A_c$ is shown in Figure 5.4 for the control case and for the four extreme cases. In most of the cases the sensitivity decreases when the BL is growing fast. This dilution however competes with the increment of average CBL depth which increases the amount of advected CO_2 (see equation 3.11). In the case of small $\Delta\theta_0$, the CBL depth starts to grow early so the average CBL depth becomes relatively large. The CBL however does

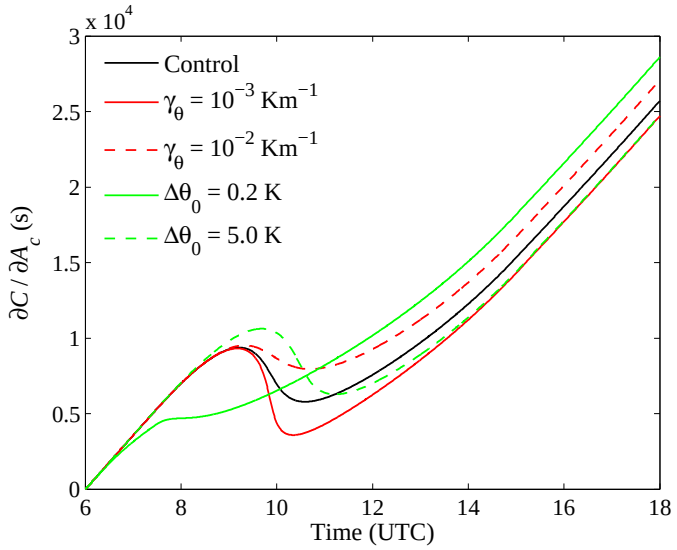

Figure 5.4: Time evolution of the sensitivity of CO_2 mixing ratio to uncertainties in CO_2 advection in five different cases. The control case has $\gamma_\theta = 3.6 \cdot 10^{-3}\,\mathrm{K\,m^{-1}}$ and $\Delta\theta_0 = 3.5\,\mathrm{K}$. In the figure legend, if the potential temperature lapse rate or inversion strength is not shown, the value for the control case applies.

not become very deep so the dilution effect is not especially strong. Therefore, there is no decrease in the sensitivity (see Figure 5.4). Large γ_θ also decreases the CBL growth so the largest sensitivities are obtained with small $\Delta\theta_0$ and large γ_θ.

Figure 5.5 shows the sensitivity of CO_2 mixing ratio to uncertainties in A_c averaged between 12 and 14 UTC as a function of $\Delta\theta_0$ and γ_θ. The largest sensitivities are obtained with low values of $\Delta\theta_0$ and large values of γ_θ. This is in agreement with the conclusion made above about the evolution of this sensitivity. Consequently, the behaviour seen in this figure can be understood with the considerations given above. It can be concluded that the averaged sensitivity of CO_2 mixing ratio to uncertainties in the CO_2 advection between 12 and 14 UTC remains small on a large range of $\Delta\theta_0$ or γ_θ.

Advection also modifies the sensitivity of CO_2 mixing ratio to errors in the CBL depth. This is illustrated in Figure 5.6 where this sensitivity is plotted for the control case with and without advection. It can be seen that the sensitivity is only slightly modified by advection. In general, if CO_2 advection is considered, this sensitivity is relatively small during midday regardless of the studied CBL as shown in Figure 5.7. At morning, this sensitivity is much larger and so are the differences between the different cases. Contribution of advection starts to be more significant at the end of day and hence the largest deviations between the different cases occur in the beginning and in the end of the simulation.

Figure 5.8 shows the sensitivity of CO_2 mixing ratio to CBL depth averaged between 12 and 14 UTC as a function of potential temperature lapse rate and initial inversion strength. Advective case is shown with coloured contours while

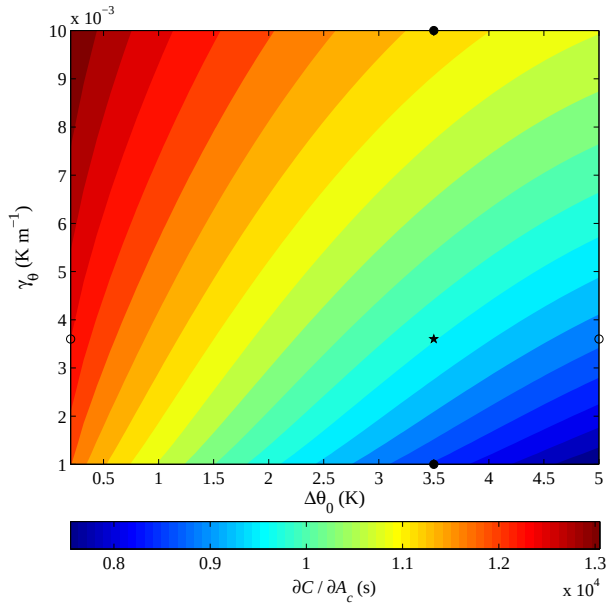

Figure 5.5: Sensitivity $\partial C/\partial A_c$ averaged between 12 and 14 UTC as a function of initial inversion strength $\Delta\theta_0$ and FA potential temperature lapse rate γ_c. The control case is shown with symbol $\star$. The rest of the symbols indicate the extreme cases considered in Figure 5.2: $\circ$'s $\Delta\theta_0 = 0.2$, and 5 K with $\gamma_\theta = 3.6 \cdot 10^{-3}$ and $\bullet$'s $\gamma_\theta = 10^{-3}$, and 10^{-2} K m^{-1} with $\Delta\theta_0 = 3.5$ K.

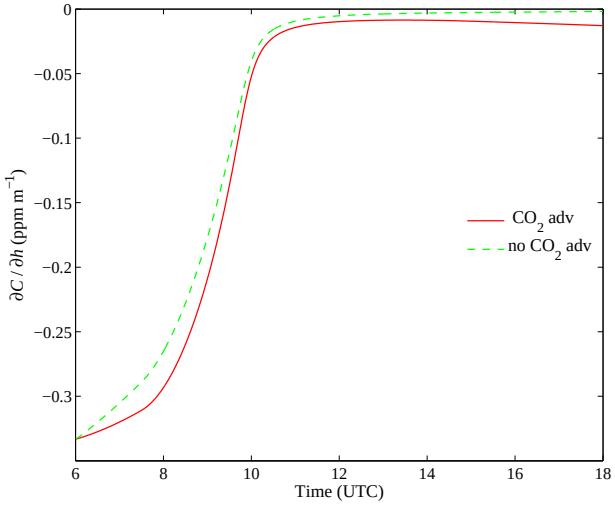

Figure 5.6: Time evolution of the sensitivity of CO_2 mixing ratio to uncertainties in CBL depth, $\partial C/\partial h$, for the control case with and without CO_2 advection.

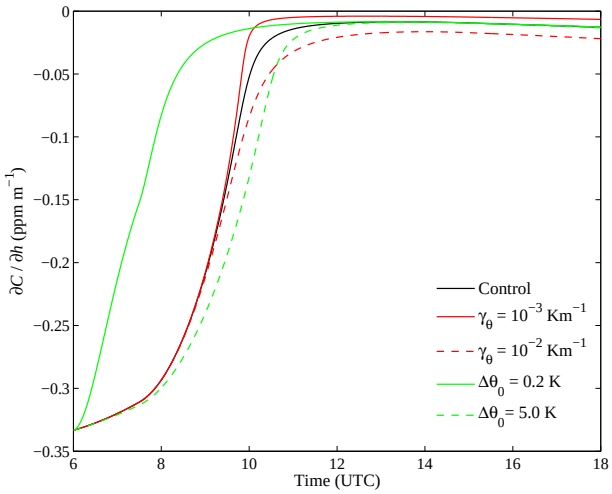

Figure 5.7: Time evolution of the sensitivity of CO_2 mixing ratio to uncertainties in the CBL depth in five different cases. The advective control case has $\gamma_\theta = 3.6 \cdot 10^{-3}\,\mathrm{K\,m^{-1}}$, and $\Delta\theta_0 = 3.5\,\mathrm{K}$. In the figure legend, if the potential temperature lapse rate or inversion strength is not shown, the value for the control case applies.

the corresponding sensitivities in the non-advective case are plotted with black line contours. In both cases the highest sensitivities occur when $\Delta\theta_0$ and γ_θ are large which is the case with the shallowest CBL. This leads to larger CO_2 mixing ratios and to larger sensitivities. Sensitivities are generally slightly more negative in the advective case and they are also nearly independent of $\Delta\theta_0$. This is due to the integral term which increases as $\Delta\theta_0$ decreases and hence the sensitivity appears to be nearly independent of $\Delta\theta_0$.

Due to the integral term appearing in equation (3.13), past errors in the CBL depth also affect the CO_2 mixing ratio. As was mentioned in Section 3 these errors cannot be estimated from equation (3.14) and no general estimation about these errors can be given without some knowledge or assumptions about the evolution of the errors in the CBL depth. If the evolution of these errors are known, the CO_2 mixing ratio uncertainty due to these errors can be estimated from equation

$$\delta C_{\langle h\rangle} = \frac{A_c - A_c^{\mathrm{FA}}}{h} \int_{t_0}^{t} \delta h(\tilde{t})\,\mathrm{d}\tilde{t} = \frac{A_c - A_c^{\mathrm{FA}}}{h}(t - t_0)\,\delta\langle h\rangle\,, \tag{5.2}$$

where δh is the time dependent error in the CBL depth, h is the simulated or estimated CBL depth at time t and $\delta\langle h\rangle = \left[\int_{t_0}^{t} \delta h(\tilde{t})\,\mathrm{d}\tilde{t}\right]/(t - t_0)$ is the time averaged error in the CBL depth. For the studied day, the error evolution, δh, is assumed to be the difference between the observed and simulated CBL depth and hence the error in C due to this error can be estimated from equation (5.2). Figure 5.9 shows the time evolution of this error (red open circles). Initial time, t_0, used in equation (5.2) was 8:10 UTC which was the time of the first

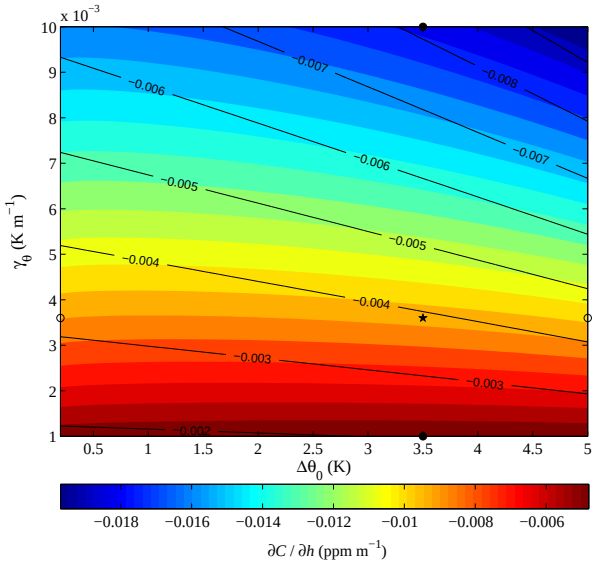

Figure 5.8: Sensitivity $\partial C/\partial h$ in the advective (coloured contours) and non-advective (black line contours) cases as a function of initial inversion strength $\Delta\theta_0$ and FA potential temperature lapse rate γ_c. The values shown in the figure are averaged between 12 and 14 UTC. The control case is shown with symbol $\star$. The rest of the symbols indicate the extreme cases considered in Figure 5.2: $\circ$'s $\Delta\theta_0 = 0.2$, and 5 K with $\gamma_\theta = 3.6 \cdot 10^{-3}$ and $\bullet$'s $\gamma_\theta = 10^{-3}$, and 10^{-2} K m^{-1} with $\Delta\theta_0 = 3.5$ K.

observation of the CBL depth. Figure 5.9 shows that the maximum error is about 1 ppm and it occurs just before 10 UTC. The maximum error occurs in the morning since there is a clear deviation between the observed and the simulated CBL depth during the morning (see Figure 5.1a) and also because the CBL depth is still shallow so the CO_2 mixing ratio is more sensitive to errors in the CBL depth.

For comparison, the green dashed line in Figure 5.9 represents the CO_2 mixing ratio error due to a constant error of 100 m in the CBL depth during the whole simulation. The CO_2 mixing ratio uncertainty remains around 1 ppm also in this case so the CO_2 mixing ratio is not extremely sensitive to past errors in the CBL depth on this day. Past errors in the CBL depth however can cause significant uncertainties in the CO_2 mixing ratios when CBL is shallow and the difference in advection between the CBL and the FA is large.

Relative sensitivities (Figure 5.3) illustrate the relative contribution of different variables on the evolution of CO_2 mixing ratio. If all the variables would have the same relative error, relative sensitivities would also describe the relative contribution of these errors on the uncertainties in the CO_2 mixing ratio. In practice, relative errors of different variables are far from being equal and hence Figure 5.3 does not correctly describe how the errors in different variables contribute to the CO_2 mixing ratio in a realistic case.

To get an idea of the CO_2 mixing ratio uncertainty due to errors in different

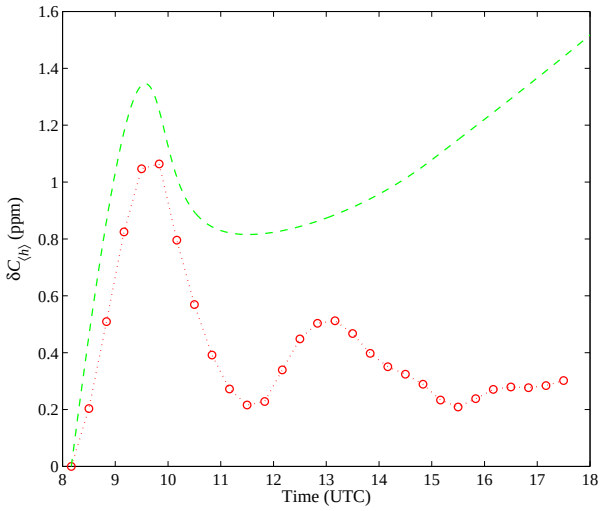

Figure 5.9: Error in the CO_2 mixing ratio due to the past uncertainties in the boundary layer depth on 25th September 2003. Red circles show the CO_2 mixing ratio uncertainty when the boundary layer depth error is calculated as the difference between the observed and simulated values (see equation 5.2 and Figure 5.1). Green dashed line represents the CO_2 uncertainty in the case of a constant error of 100 meters in boundary layer depth.

variables, a plausible magnitude of error has to be estimated for all the variables. Error in the initial CO_2 mixing ratio, δC_0, is assumed to be of the order of 1 ppm. In general, CO_2 mixing ratios can be measured more accurately but the average ML value of initial CO_2 mixing ratio can have larger errors, for example if the measurements are taken only at few heights before the morning transition. Initial FA CO_2 mixing ratio is also assumed to have a similar error of 1 ppm, even though it is generally more challenging to measure mixing ratios in the FA than in the ML. CO_2 mixing ratio lapse rate in the FA is sometimes taken to be zero in the simulations [26] so its error is estimated to be of the order of its magnitude, $\delta\gamma_c \approx \gamma_c = 3 \cdot 10^{-3}\,\mathrm{ppm\,m^{-1}}$. The error in the initial and instantaneous boundary layer depth is estimated to be of the order of 50 m throughout the day. This error of course depends on the method that is used to determine boundary layer depth but for example Driedonks [76] calculated that the error made by acquiring the boundary layer depth from an individual radiosounding can be as much as ± 100 m. In general, the error can also be time dependent but for simplicity a constant error is considered here. Error in the CO_2 surface flux is estimated as an average deviation of the observed values from the prescribed value used in the MLM simulation. This gives an error of $0.05\,\mathrm{ppm\,m\,s^{-1}}$ which is half of the diurnal maximum. Advection in the boundary layer and in the FA is often neglected when they are relatively small so the error in these variables is estimated to be $10^{-5}\,\mathrm{ppm\,s^{-1}}$ which would correspond to a relatively small advection. The estimated magnitudes of errors are summarized in Table 5.2.

Figure 5.10 illustrates the errors in the CO_2 mixing ratio due to the un-

Table 5.2: Estimated magnitudes of errors in different variables. Error $\delta\langle\overline{w'c'}\rangle_s$ is used only in the calculation of CO_2 mixing ratio uncertainty while δC is employed in the calculation of the inferred CO_2 surface flux uncertainty.

Error	Estimated magnitude
δC_0 (ppm)	1
δC_0^{FA} (ppm)	1
δC (ppm)	1
$\delta\gamma_c$ (ppm m^{-1})	$3{\cdot}10^{-3}$
δh (m)	50
δh_0 (m)	50
$\delta\langle\overline{w'c'}\rangle_s$ (ppm m s^{-1})	0.05
δA_c (ppm s^{-1})	10^{-4}
δA_c^{FA} (ppm s^{-1})	10^{-4}

certainties shown in Table 5.2. Errors are calculated by multiplying the corresponding absolute value of the sensitivity with the error shown in Table 5.2, except $\delta C_{\langle h\rangle}$ which is calculated from equation (5.2). After midday the contribution of each error is quite similar. This emphasizes the fact that in reality the errors in all the variables can be significant even if their relative sensitivity would be small, and vice versa. For example, initial CO_2 mixing ratio is one of the most important variables in determining the CO_2 mixing ratio evolution (see Figure 5.3) but generally, it can be determined quite accurately and hence its error might not cause significant uncertainty on the CO_2 mixing ratio in the afternoon. Furthermore, the error in advection in the CBL causes the largest uncertainty to the CO_2 mixing ratio at the end of the simulation even though a relative small error in advection is considered. This shows that neglecting even quite mild advection can cause significant error on the CO_2 mixing ratio already on diurnal time scales.

Time evolution of CO_2 mixing ratio is influenced by h and h_0 in an opposite way (see Figure 5.3). In practice, the large uncertainties due to these errors in the morning would partly cancel each other since the errors in h and h_0 are most likely to be correlated during the morning. As it was noted earlier, the CO_2 mixing ratio is also not linear with h and h_0 and thus the errors δC_h and δC_{h_0} shown in Figure 5.10 are approximative. However, Figure 5.10 is not supposed to give a general picture about the errors but to illustrate that the errors in variables with small relative sensitivities can lead to large uncertainties in the CO_2 mixing ratio. Advection, FA CO_2 mixing ratio lapse rate and CO_2 surface flux have often large relative errors and hence their contribution to CO_2 mixing ratio uncertainty is underestimated if only relative sensitivities are considered.

5.1.3 Inferred CO_2 surface flux uncertainties

Sensitivity of the inferred CO_2 surface flux to errors in different CBL variables ϕ is compared by normalizing equations (3.16)-(3.23) as

$$RSF_\phi = \frac{\partial\langle\overline{w'c'}\rangle_s}{\partial\phi}\cdot\frac{\phi}{\langle\overline{w'c'}\rangle_s}. \tag{5.3}$$

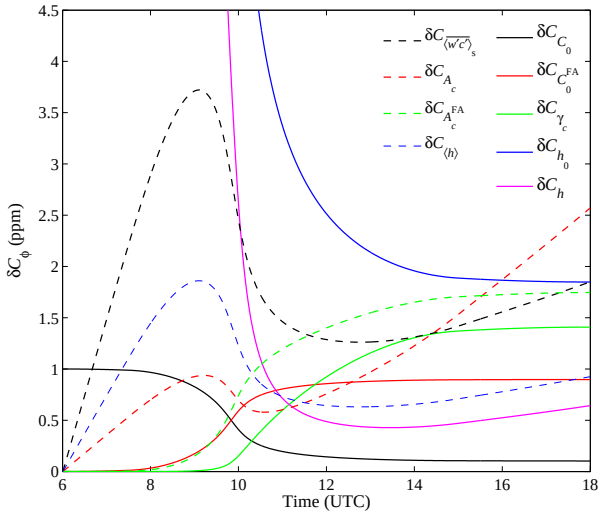

Figure 5.10: Errors in the CO_2 mixing ratio due to errors in different boudary layer variables. Errors used in the calculation are shown in Table 5.2.

Time evolution of the relative sensitivities calculated from equation (5.3) are shown in Figure 5.11 for the control case. Advection in the CBL only alters the sensitivities $\partial\langle\overline{w'c'}\rangle_s/\partial A_c$ and $\partial\langle\overline{w'c'}\rangle_s/\partial h$. Relative sensitivity RSF_{A_c} is however really small compared to the other sensitivities so advection has only a minor effect on the inferred CO_2 surface flux on daily time scales.

Figure 5.12 plots the sensitivity of the inferred CO_2 surface flux to uncertainties in A_c averaged between 12 and 14 UTC as a function of $\Delta\theta_0$ and γ_θ. The inferred CO_2 surface flux is most sensitive to uncertainties in the CO_2 advection when $\Delta\theta_0$ and γ_θ are small. Small values of $\Delta\theta_0$ and γ_θ leads to large CBL depth which increases the contribution of advection in the CO_2 budget. Correspondingly, the errors made in the estimation of advection causes larger errors on the inferred CO_2 surface flux. It can be also noted that the change in this sensitivity is relatively large within the studied range of $\Delta\theta_0$ and γ_θ.

Figure 5.13 shows the sensitivity of the inferred CO_2 surface flux to uncertainties in the CBL depth for the advective (coloured contours) and non-advective (black contours) cases averaged between 12 and 14 UTC as a function of $\Delta\theta_0$ and γ_θ. In the advective case this sensitivity has its largest values when $\Delta\theta_0$ is small and γ_θ is large. Low CBL depth caused by large γ_θ leads to large CO_2 mixing ratio and this increases the sensitivity since the sensitivity is proportional to the CO_2 mixing ratio (see equation (3.23)). Due to advection a small $\Delta\theta_0$ also leads to large CO_2 mixing ratios after midday (see Figure 5.2) and therefore the largest sensitivities between 12 and 14 UTC are obtained with small $\Delta\theta_0$ and large γ_θ. However, the changes in this sensitivity are relatively small within the studied parameter range and hence the average sensitivity between 12 and 14 UTC depends only weakly on $\Delta\theta_0$ and γ_θ.

An interesting feature in Figure 5.13 is that the sensitivity $\partial\langle\overline{w'c'}\rangle_s/\partial h$ has a local minimum as a function of γ_θ. This minimum results from the interplay of the first and third terms of equation (3.23). The first term is the CO_2 mixing

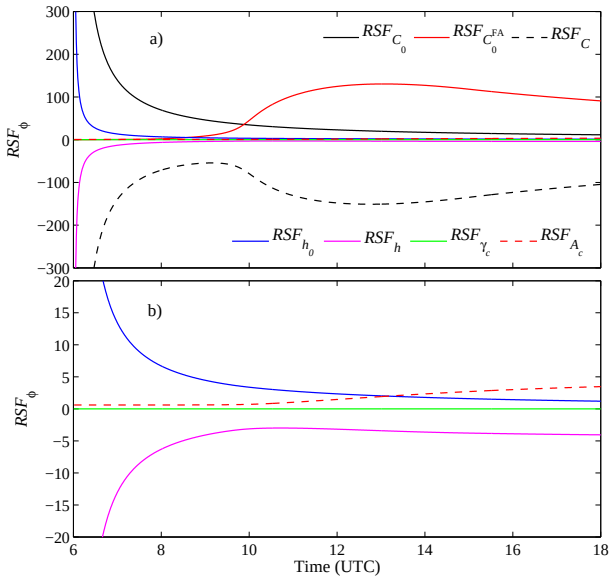

Figure 5.11: Time evolution of the normalized sensitivities of the inferred CO_2 surface flux to a) all CBL variables except A_c^{FA} for the control case and b) a detail of a).

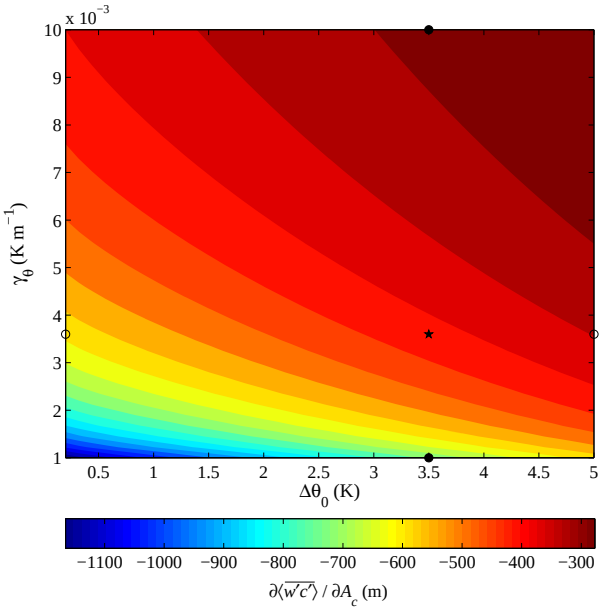

Figure 5.12: Same as Figure 5.5 for $\partial\langle\overline{w'c'}\rangle_{\mathrm{s}}/\partial A_c$.

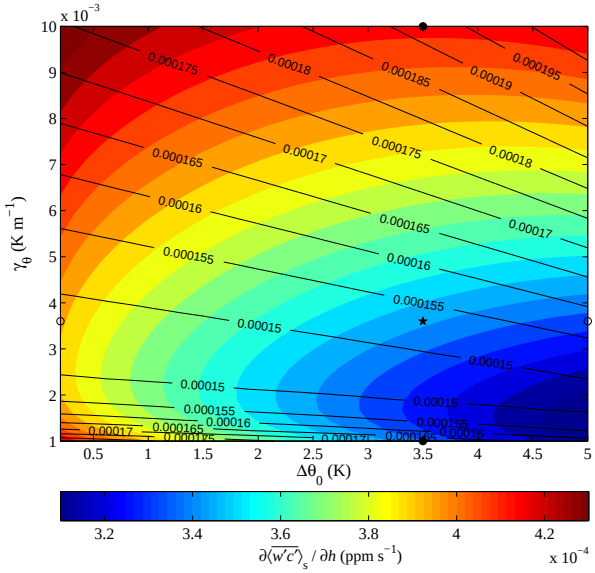

Figure 5.13: Same as Figure 5.5 for $\partial\langle\overline{w'c'}\rangle_s/\partial h$.

ratio which increases with increasing γ_θ. The third term is proportional to the CBL depth and because of the negative sign of γ_c, this term decreases with increasing γ_θ. Thus the minimum is caused by the first and the third terms which increase in the opposite directions.

Sensitivity of the inferred CO_2 surface flux to errors in the CBL depth in the non-advective case is shown as black contours in Figure 5.13. In this case the largest sensitivities occur when both $\Delta\theta_0$ and γ_θ are large. This is because large $\Delta\theta_0$ and γ_θ suppresses the CBL growth and in the absence of advection the largest CO_2 mixing ratios occur when the CBL depth is small. Large CO_2 mixing ratio instead increases the sensitivity of the inferred CO_2 on the CBL depth as can be seen from equation (3.23). The inclusion of CO_2 advection hence clearly changes the dependence of this sensitivity on the CBL variables.

Inferred CO_2 surface flux is also affected by the history of the errors in the CBL depth. Error in the inferred CO_2 surface flux due to the past errors in the CBL depth can be calculated as

$$\delta\langle\overline{w'c'}\rangle_{s,\langle h\rangle} = \frac{A_c^{\mathrm{FA}} - A_c}{t - t_0}\int_{t_0}^{t}\delta h(\tilde{t})\,\mathrm{d}\tilde{t} = (A_c^{\mathrm{FA}} - A_c)\,\delta\langle h\rangle\,, \tag{5.4}$$

if the time evolution of the CBL depth error, $\delta h(t)$, is known. Red circles in Figure 5.14 show the evolution of the inferred CO_2 surface flux error for the advective control case when the error in the CBL depth is assumed to be the difference between the observed and simulated values. Time evolution of this error is similar as in Figure 5.9 due to the same error evolution of the CBL depth but the error is relatively much larger for the inferred CO_2 surface flux than for the CO_2 mixing ratio. The maximum error of about 0.04 ppm m s^{-1} occuring before 10 UTC is about 60% of the instantaneous CO_2 surface flux and 40% of the maximum value of the surface flux during the day. Green dashed

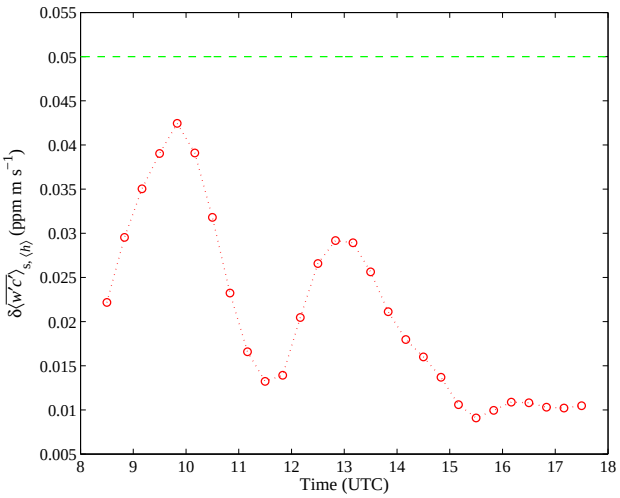

Figure 5.14: Error in the inferred CO_2 surface flux due to the past uncertainties in the CBL depth on 25th September 2003. Dashed line is the uncertainty in the case with constant error of 100 meters in CBL depth. Red circles show the inferred CO_2 surface flux uncertainty when the CBL depth error is calculated as the difference between the observed and simulated values.

line in Figure 5.14 shows that uncertainty in the CO_2 surface flux is half of the daily maximum during the whole day when the CBL depth has a continuous error of 100 meters. History dependent errors can hence cause really significant uncertainties in the inferred CO_2 surface flux even when the CO_2 advection in the CBL is relatively small.

As was discussed in the case of CO_2 mixing ratio, relative sensitivities do not properly describe relative contribution of different errors since in reality the relative errors of different variables are completely different. Thus it is useful to consider errors in the inferred CO_2 surface flux due to plausible errors in different variables. Figure 5.15 shows these uncertainties for the errors shown in Table 5.2. Most of the errors are roughly equal in magnitude after midday but δC_0 is much smaller than the other errors. In addition, δh_0 is a bit larger than the other errors. Moreover, advection in the CBL is again the largest source of error at the end of the day. These conclusions are similar to those made for the corresponding errors of CO_2 mixing ratio. It again illustrates that it is difficult to estimate the contribution of different errors only from the relative sensitivities.

5.1.4 Effect of CO_2 conditions on the sensitivities

Sensitivity of CO_2 mixing ratio to errors in the CBL variables is also affected by the CO_2 profile in the FA, not just by the potential temperature profile considered above. Therefore, a sensitivity analysis is also conducted for the initial CO_2 mixing ratio jump, ΔC_0, and CO_2 mixing ratio lapse rate, γ_c. This was done by performing 41×41 MLM simulations with ΔC_0 and γ_c ranging from $\Delta C_0 \in [-50, -10]$ (ppm) and $\gamma_c \in [-0.01, 0]$ (ppm m^{-1}) respectively. Unlike the

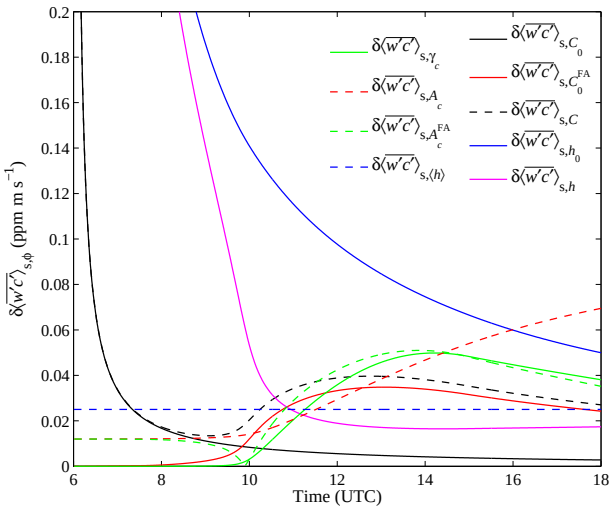

Figure 5.15: Errors in the inferred CO_2 surface flux due to errors in different variables. Errors used in the calculation are shown in Table 5.2.

potential temperature variables $\Delta\theta_0$ and γ_θ, the corresponding CO_2 variables $\Delta C_0 = C_0^{\mathrm{FA}} - C_0$ and γ_c appear explicitly in equations (3.5), (3.10) and (3.13), and therefore their contribution can be seen more directly from these equations.

Evolution of the sensitivities $\partial C/\partial h$ and $\partial C/\partial h_0$ are plotted in Figure 5.16 for five different cases. The first case is the control case ($\Delta C_0 = -40\,\mathrm{ppm}$, $\gamma_c = -0.003\,\mathrm{ppm\,m}^1$) and in the other four cases the values of ΔC_0 and γ_c are changed from the control case to one of the extreme values considered in the sensitivity analysis. During the morning, the initial CO_2 mixing ratio jump, ΔC_0, influences the sensitivities much more than the CO_2 mixing ratio lapse rate, γ_c. Although it cannot be seen from Figure 5.16, it turns out that during midday and afternoon γ_c affects the sensitivities approximately as much as ΔC_0. This conclusion is supported by Figure 5.17 which shows the average sensitivity of CO_2 mixing ratio to uncertainties in the CBL depth between 12 and 14 UTC as a function of ΔC_0 and γ_c. It can be seen that similar relative changes in ΔC_0 and γ_c causes similar changes in the sensitivity.

Different CO_2 conditions in the FA changes also the sensitivity $\partial C/\partial h$ shown in Figure 5.8. The value of $\Delta C_0 + \gamma_c h_0/2$ changes the relative importance of h^{-2}-terms in equation (3.13). Therefore, a change in the values of ΔC_0 and γ_c alters the dependence of $\partial C/\partial h$ on the CBL dynamics. For example, if ΔC_0 is set to $-10\,\mathrm{ppm}$, the contours in Figure 5.8 become nearly horizontal. It should be noted that even though the CO_2 conditions in the FA modify the sensitivities $\partial C/\partial h$ and $\partial C/\partial h_0$, the corresponding relative sensitivities are small.

Sensitivities $\partial\langle\overline{w'c'}\rangle_{\mathrm{s}}/\partial h_0$ and $\partial\langle\overline{w'c'}\rangle_{\mathrm{s}}/\partial h$ also depend on the CO_2 conditions in the FA. Time evolution of these sensitivities is plotted in Figure 5.18 for the same cases that were considered in Figure 5.16. General conclusions about these two figures are similar. That is, during the morning the initial CO_2 mixing ratio jump ΔC_0 has a larger impact on the considered sensitivities but during midday and afternoon the CO_2 mixing ratio lapse rate γ_c contributes

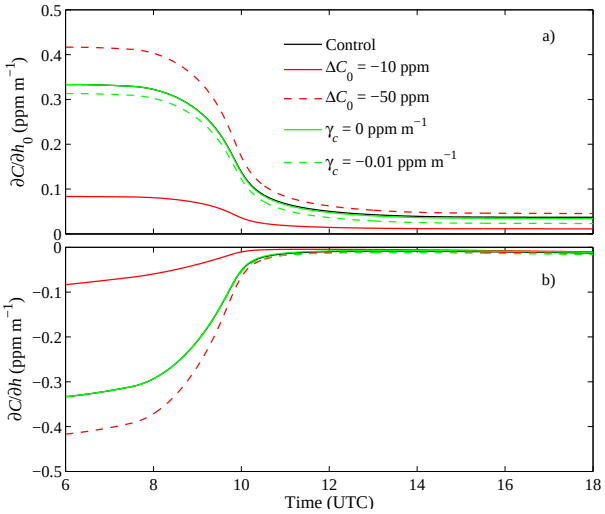

Figure 5.16: Time evolution of the sensitivity of CO_2 mixing ratio to uncertainties in a) initial CBL depth and b) instantaneous CBL depth plotted for five different cases. The control case has $\gamma_c = -3 \cdot 10^{-3}$ ppm m^{-1}, and $\Delta C_0 = -40$ ppm. In the figure legend, if the CO_2 mixing ratio lapse rate or the CO_2 inversion jump is not shown, the value for the control case applies.

to the sensitivities approximately as much as ΔC_0. This can be seen from Figure 5.17 where black line contours show the averaged sensitivity of the inferred CO_2 surface flux between 12 and 14 UTC as a function of ΔC_0 and γ_c.

A change in the values of ΔC_0 and γ_c have also an impact on the shape of the contours plotted in Figure 5.13. Even though the FA CO_2 conditions change the sensitivities $\partial\langle\overline{w'c'}\rangle_s/\partial h_0$ and $\partial\langle\overline{w'c'}\rangle_s/\partial h$, the corresponding relative sensitivities are small especially during the midday. Consequently, the main conclusions given above for the studied day hold also for other days with different CO_2 conditions in the FA.

5.1.5 Effect of advection in the free atmosphere

Thus far the CO_2 advection was included only in the CBL. In the general, case CO_2 can also be advected in the FA and hence the effect of this advection on the CO_2 mixing ratio evolution is next considered. Advection in the FA changes the CO_2 mixing ratio evolution only through entrainment and hence it has no impact on the CO_2 mixing ratio in the CBL if the CBL is not growing. Moreover, if advection is equal in the CBL and in the FA, the evolution of CO_2 entrainment is the same as in the non-advective case.

Figure 5.19 shows the CO_2 mixing ratio evolution (a) and CO_2 entrainment flux (b) in four different advection cases. In all the cases the sum of A_c and A_c^{FA} is 1.8 ppm h^{-1}. In the general case where advection in the ML and in the FA are different, $A_c = 1.0$ ppm h^{-1} and $A_c^{FA} = 0.8$ ppm h^{-1} were prescribed. Figure 5.19a shows that the case with no advection in the CBL (FA adv, purple line) has the lowest CO_2 mixing ratio at the beginning and at the end of the

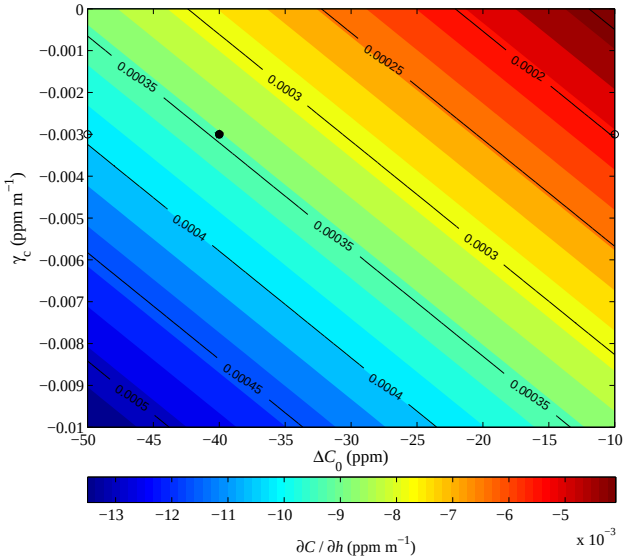

Figure 5.17: Sensitivity of $\partial C/\partial h$ (coloured contours) and $\partial\langle\overline{w'c'}\rangle_s/\partial h$ (black contours) as a function of initial CO_2 mixing ratio jump ΔC_0 and CO_2 mixing ratio lapse rate γ_c. The values shown in this figure are averaged between 12 and 14 UTC. The control case is shown with symbol $\star$. The rest of the symbols indicate the extreme cases considered in Figures 5.16 and 5.18: $\circ$'s $\Delta C_0 = -50$, and $= -10$ ppm with $\gamma_c = -3\cdot10^{-3}$ ppm m^{-1} and $\bullet$'s $\gamma_c = 0$, and 10^{-2} ppm m^{-1} with $\Delta C_0 = -40$ ppm.

simulation when the CBL is growing really slowly and hence the CO_2 advected into the FA does not enter into the ML. During the fast CBL growth, this case, instead, has the highest CO_2 mixing ratios since the dilution of CO_2 concentration through entrainment is smaller. This can be clearly seen from Figure 5.19b. Hence, advection in the FA has the tendency to flatten out the changes in the CO_2 mixing ratio when CO_2 advection is positive and the initial CO_2 jump is negative. Advection in the CBL instead amplifies the change in the CO_2 mixing ratio and the other studied advection cases are between these two extreme cases.

5.1.6 Effect of large scale subsidence

Large scale subsidence was neglected in the sensitivity analysis in order to get an analytical formula for the CO_2 mixing ratio evolution. Subsidence is sometimes neglected when diurnal time scales are simulated, partly because it is difficult to determine its value accurately. Subsidence however changes the entrainment velocity and entrainment fluxes, and hence it also changes the evolution of the CO_2 mixing ratio and the inferred CO_2 surface flux. Therefore, it is interesting to estimate the magnitude of the errors when subsidence is neglected.

Subsidence can be easily included in the MLM simulation but an analytical formula for the CO_2 mixing ratio evolution was not obtained. Influence of

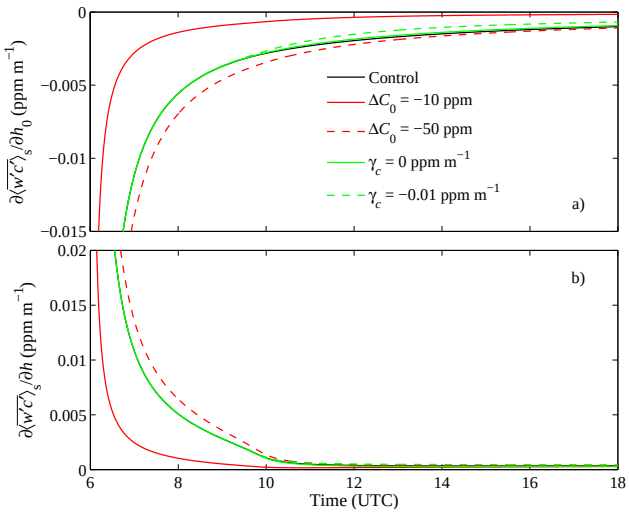

Figure 5.18: Time evolution of the sensitivity of inferred CO_2 surface flux to uncertainties in a) initial CBL depth and b) instantaneous CBL depth in five different cases. The control case has $\gamma_c = -3 \cdot 10^{-3}$ ppm m^{-1}, and $\Delta C_0 = -40$ ppm. In the figure legend, if the CO_2 mixing ratio lapse rate or the CO_2 inversion jump is not shown, the value for the control case applies.

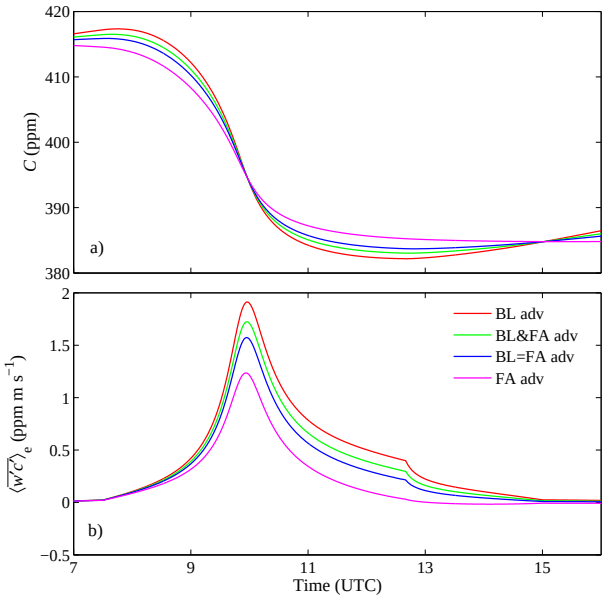

Figure 5.19: a) CO_2 mixing ratio evolution and b) CO_2 entrainment in different advection conditions in the ML and in the FA for the control case. The sum of advection in the ML and in the FA is 1.8 ppm h^{-1} in all of the cases. Discontinuities in the CO_2 entrainment just before 13 UTC are due to the change in the prescribed value of γ_c (see Table 5.1).

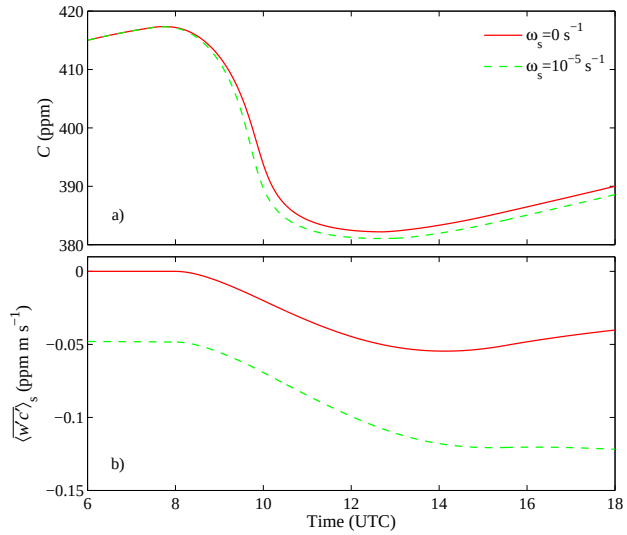

Figure 5.20: a) CO_2 mixing ratio evolution and b) time averaged inferred CO_2 surface flux evolution is compared for simulations with and without large scale divergence.

subsidence is investigated only by comparing two numerical simulations so that the magnitude of errors due to neglection of subsidence can be addressed. Figure 5.20a compares the evolution of CO_2 mixing ratio for the cases with zero and non-zero large scale divergence. Initial and prescribed values shown in Table 5.1 are used in these MLM simulations. In the MLM simulations, subsidence, w_s, is calculated from the large scale divergence, ω_s according to equation (2.29). Large scale diverge of $\omega_s = 10^{-5}\,s^{-1}$ was prescribed on the second simulation and hence the subsidence velocity after midday is about $1\,cm\,s^{-1}$.

Inclusion of subsidence decreases the CO_2 mixing ratio (see Figure 5.20a) on the studied day. The difference in the CO_2 mixing ratio between the two simulations is more than 1 ppm after about 9 UTC and a maximum value of about 4 ppm occurs around the time of the maximum growth rate of the CBL, that is around 10 UTC. The difference in the CBL depth starts to be significant only after about 13 UTC (not shown) so the decrease in CO_2 mixing ratio is mostly due to differences in the CO_2 entrainment. Figure 5.20b shows the corresponding plot for the time averaged inferred CO_2 surface flux. Time averaged inferred CO_2 surface flux differs about $0.05\,ppm\,ms^{-1}$ between the two cases during the whole day. This is about half of the diurnal maximum of the flux so the difference is indeed significant. Figure 5.20 thus illustrates that an error of $10^{-5}\,s^{-1}$ in large scale divergence can lead to significant errors in the CO_2 mixing ratio and in the inferred CO_2 surface flux even on diurnal time scales.

5.2 12th March 2004

The second analyzed day is 12th March 2004 which was characterized by low heat advection and large CO_2 advection. South Easterly winds of about 8-

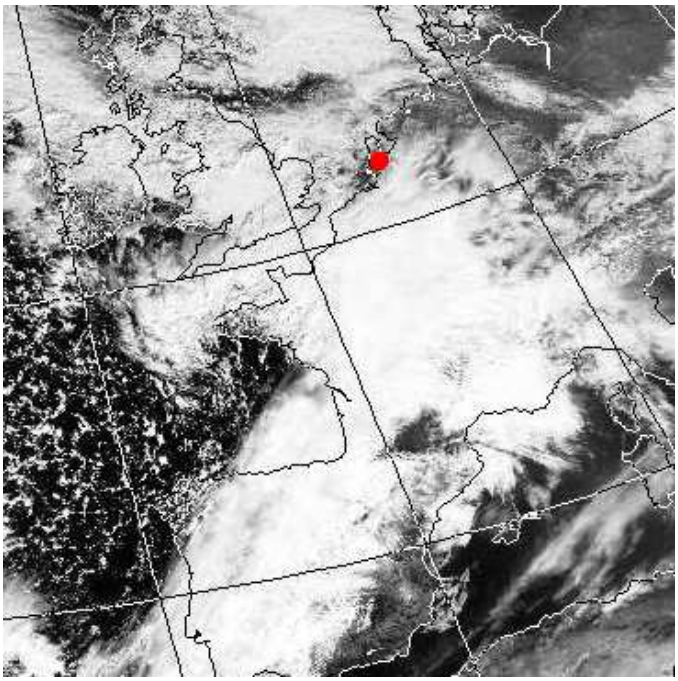

Figure 5.21: Satellite picture on a visible wavelengths (0.58-0.68 µm) taken at 11:19 UTC on 12th March 2004 [78]. Approximate location of Cabauw is marked with a red dot. Regions South of Cabauw were largely covered with clouds.

$10\,\mathrm{m\,s^{-1}}$ was measured during the day and moisture ranged from 3 to $4\,\mathrm{g\,kg^{-1}}$. Casso *et al.* found that the previous night was weakly stratified due to the constant and high velocity winds [28]. The day was clear but occasional clouds was observed. A satellite picture in Figure 5.21 shows that the regions South of Cabauw were largely covered with clouds but the Cabauw region was relatively clear. This heterogeneity in the cloud cover could at least partially explain the observed CO_2 advection. Cloud cover decreases the solar radiation reaching the ground. Consequently, sensible and latent heat fluxes decreases which leads to shallower CBL and higher CO_2 mixing ratios. Reduced solar radiation also decreases the CO_2 uptake by vegetation and hence causes elevated CO_2 mixing ratios. For example, Chan *et al.* [77] found that the CO_2 flux variations due to meteorological conditions are typically larger than the CO_2 variations due to the heterogeneity. The heterogeneity in the cloud cover could thus explain the advection of CO_2 to the Cabauw region from the South-East during this day. More detailed description of the general conditions during this day is given in [28]. This second day was chosen to be analyzed because it actually has significant CO_2 advection unlike the first analyzed day. It is also used to compare the sensitivities between different days and to show the applicability of the framework on different days.

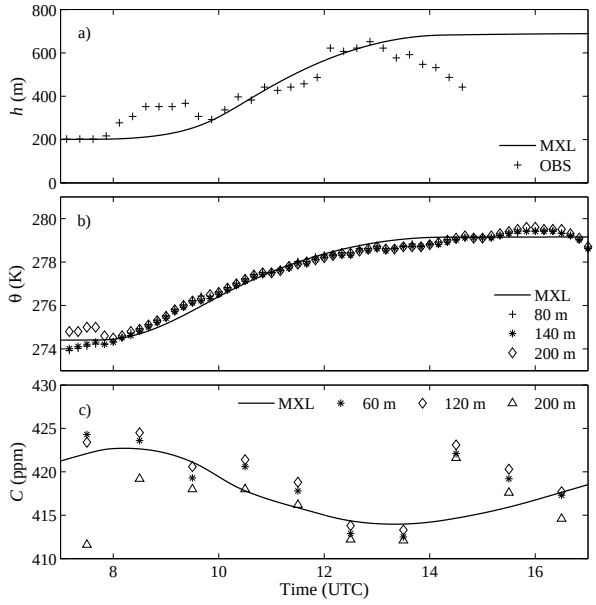

Figure 5.22: Observed (symbols) diurnal evolution of a) CBL depth, b) potential temperature and c) CO_2 mixing ratio on 12th March 2004 together with the corresponding evolutions obtained from the MLM simulations (solid line). Initial and prescribed values of the MLM simulation are shown in Table 5.3.

5.2.1 Mixed-layer simulation

Diurnal evolution of CBL variables were again simulated with the MLM. Initial and prescribed values used in the MLM simulation are based on the observations taken at Cabauw and they are presented in Table 5.3. It should be noted that even though the form of the prescribed advection is quite complicated, it is not fully arbitrary. Instead, it is roughly fitted to the observed evolution of CO_2 mixing ratio and to the CO_2 budget [28]. Diurnal evolution of CBL depth, potential temperature and CO_2 mixing ratio obtained from the MLM simulation are shown in Figure 5.22 together with the observations taken at Cabauw. MLM simulation reproduce the evolution of potential temperature moderately well but there are notable deviations between the simulated and observed evolution of CBL depth and CO_2 mixing ratio between 8 and 10 UTC and after 13 UTC. However, between 10 and 13 UTC the simulation results compare satisfactory with the observations.

5.2.2 Horizontal and vertical advection

Casso *et al.* [28] argued that the CO_2 mixing ratio remained roughly constant during the day. Figure 5.22c however illustrates that this was not case. Instead, the CO_2 mixing ratio first decreased about 10 ppm and then exhibited a clear jump around 14:30 UTC. This jump was not distinct in their plot since they

Table 5.3: Initial and prescribed values used for the MLM based on the observations taken at Cabauw (The Netherlands) on 12th March 2004. Time t is given in seconds and it ranges from zero to 44100 s.

Property	Value
CBL layer properties	
Initial CBL layer depth, h_0 (m)	200
Large scale subsidence velocity, w_s ($m\,s^{-1}$)	0
Heat	
$\overline{w'\theta'}\|_s$, (07:45-14:15 UTC) ($K\,m\,s^{-1}$)	$0.09\,\sin\left(\frac{\pi(t-8100)}{23400}\right)$
Entrainment to surface sensible flux ratio, β	0.25
θ_0 (K)	274.4
$\Delta\theta_0$ (K)	2.0
γ_θ ($K\,m^{-1}$)	$8{\cdot}10^{-3}$
Moisture	
$\overline{w'q'}\|_s$, (05:30-17:45 UTC) ($g\,kg^{-1}\,m\,s^{-1}$)	$0.028\,\sin\left(\frac{\pi t}{44100}\right)$
q_0 ($g\,kg^{-1}$)	3.05
Δq_0 ($g\,kg^{-1}$)	-0.9
γ_q ($g\,kg^{-1}\,m^{-1}$)	0
Carbon dioxide	
$\overline{w'c'}\|_s$, (07:30-16:00 UTC) ($ppm\,m\,s^{-1}$)	$-0.25\,\sin\left(\frac{\pi(t-7200)}{30600}\right)$
C_0 (ppm)	419.5
ΔC_0 (ppm)	-15.5
γ_c ($ppm\,m^{-1}$)	0
A_c ($ppm\,s^{-1}$)	
$t < 3600$ s	$\frac{5{\cdot}10^{-4}}{3600}t$
$3600\,\text{s} \leq t < 9000$ s	$5{\cdot}10^{-4}$
$9000\,\text{s} \leq t < 14400$ s	$\frac{9{\cdot}10^{-4}}{5400}(t\text{-}900) + 5{\cdot}10^{-4}$
$14400\,\text{s} \leq t < 18000$ s	$14{\cdot}10^{-4}$
$18000\,\text{s} \leq t < 23400$ s	$\frac{-9{\cdot}10^{-4}}{5400}(t\text{-}23400) + 5{\cdot}10^{-4}$
$t \geq 23400$ s	$5{\cdot}10^{-4}$
A_c^{FA} ($ppm\,s^{-1}$)	0

used 5-point running average and a large range on the vertical axis. Figure 5.22a suggests that the CBL depth significantly decreased around the time of the CO_2 mixing ratio jump and hence it would be questionable to link the increase in the CO_2 mixing ratio only to advection.

Casso *et al.* deduced the advection from the ML budget equation which assumes that the CO_2 mixing ratio is constant with height and that the vertical fluxes are linear in the CBL. The observed CO_2 mixing ratio jump however occurs around sunset when the sensible heat fluxes are nearly zero and hence these assumptions might not be valid during this time. Casso *et al.* took into account the nonlinearity of the fluxes in their analysis but they only considered the lower part of the atmosphere where the measurements were taken. Flux linearity in the lower part of the atmosphere however does not necessarily guarantee the linearity in the whole CBL during sunset when turbulence starts to decay. Therefore their conclusions regarding to the CO_2 advection are slightly questionable during and after sunset. The discrepancies between the ML analysis and observations suggests that the ML assumptions were not attained after about 15:30 UTC. Non-convectiveConsequently, the following analysis focus mainly on the preceding time period.

Advection retrieved from the net ecosystem-atmosphere exchange (NEE) calculations (see for example [52]) or from the budget method used by Casso *et al.* [28] cannot distinguish between vertical and horizontal advection. The current version of the MLM can only describe horizontal advection and thus it would be desirable to have an idea if the CO_2 advection was mainly vertical or horizontal. Horizontal advection depends on the horizontal wind speed and hence the contribution of horizontal advection on the total advection can be examined by comparing the evolution of the total advection and the height integral of the horizontal wind speed (IU) [52]:

$$\mathrm{IU} = \int_{z_1}^{z_2} \overline{u}\,\mathrm{d}z\,, \tag{5.5}$$

where $\overline{u}$ is the horizontal wind velocity, and z_1 and z_2 are the vertical limits of integration. If horizontal advection is dominating and horizontal CO_2 gradient remains approximately constant in time, the total advection should correlate with IU. Figure 5.23 qualitatively shows that the total advection and IU in the upper part of the tower (120-200 m) are correlated during the day approximately from 8:30 till 12:30 UTC. Outside this period the correlation between them is poor. In addition, the correlation in the lower part of the tower is relatively poor compared to the upper part (not shown). These findings are similar to the ones obtained by Yi *et al.* [52] for the tall tower in Wisconsin during July 1997. It is thus likely that the advection is mainly horizontal between 8:30 till 12:30 UTC but during other times vertical advection might have played an important role.

Even if the total advection would be dominated by horizontal advection the correlation between advection and IU remains strong only if horizontal CO_2 gradient remains approximately constant. This assumption cannot be verified with the tower measurements. However, wind patterns and spatial evolution of moisture and temperature during this day could be investigated by simulating the day with the MM5 mesoscale model. For the simulation, four nested domains were defined with resolutions of 27, 9, 3 and 1 km, respectively. The biggest

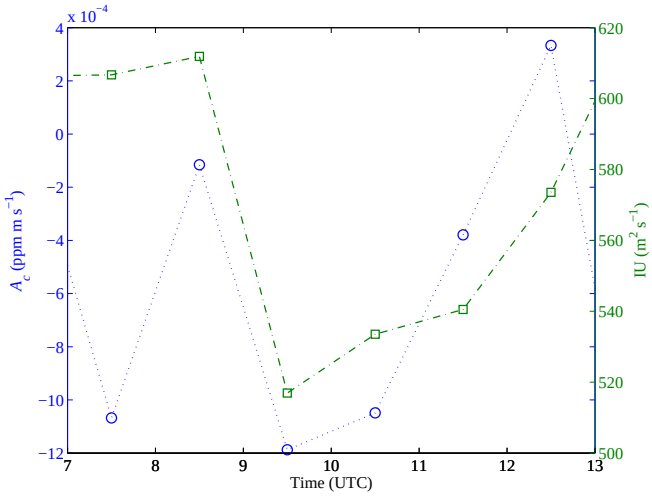

Figure 5.23: Time evolution of total CO_2 advection and the height integral of horizontal wind speed (IU) in the upper part of the tower (120-200 m). Dotted and dash-dotted lines are guides to the eye.

domain was centered at 51.97 °N, 4.92 °E. The initial and boundary conditions were updated every six-hours with the analysis of the European Centre for Medium-Range Weather Forecasts model (ECMWF).

Simulation results indicate that a front with significant humidity difference reached the Cabauw region around the time when the CO_2 mixing ratio jump was observed. This is illustrated in Figure 5.24 where vertical cross sections of water vapour mixing ratio obtained from the MM5 simulation are shown at different times. MM5 model does not include CO_2 so it could not be ensured if this front was accompanied with CO_2 advection. However, a front with notable CO_2 difference entering the Cabauw region would be a likely explanation to the sudden jump in the CO_2 mixing ratio. This would also cause a non-constant horizontal CO_2 gradient which could explain the poor correlation of advection with the horizontal wind speed at the end of the day. Therefore, horizontal advection could have been significant at the end of the day despite the poor correlation between advection and IU.

Estimation of vertical advection is really difficult since mean vertical velocity is usually small compared to the systematic errors of the measurement [1, 79]. One way to examine if the total advection could be only due to vertical advection is to calculate the magnitude of mean vertical wind velocity required to produce the observed total advection [52]. This analysis shows that the required mean vertical wind in the upper part of the tower speed remained around -0.02 $m\,s^{-1}$ till about 8:30 UTC. This is a plausible value for large scale subsidence and the decrease in the CBL depth after sunset indeed suggests that large scale subsidence could have been present during the day. Later on the day the mean vertical wind velocity necessary to produce the observed advection is unreasonably large due to the small vertical CO_2 gradients occuring in the well-mixed CBL. However, the required mean vertical wind velocity remained large even

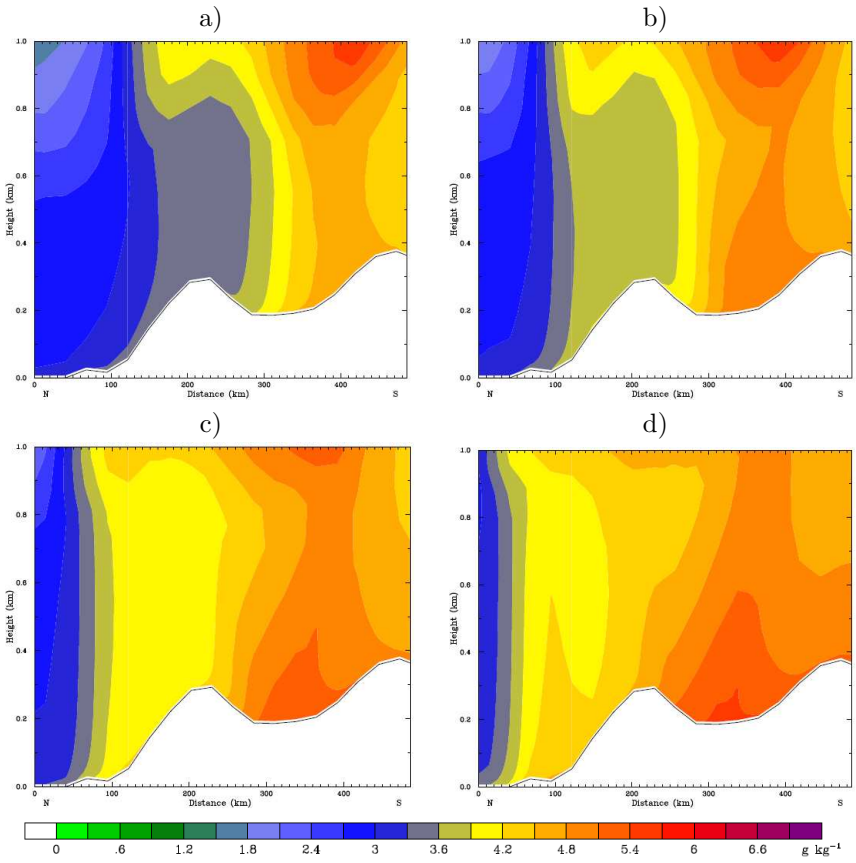

Figure 5.24: Vertical cross sections of water vapour mixing ratio at a) 10:59 UTC, b) 12:00 UTC and c) 13:00 UTC and d) 13:59 UTC on 12th March 2004. Cross section are obtained from a MM5 simulation. Horizontal axis shows the distance from the Cabauw meteorogical tower (51.651 °N, 5.099 °E) to south up to 47.172 °N, 5.099 °E.

in the end of the day which indicates that the vertical advection alone did not account for the large jump in the CO_2 mixing ratio. Therefore the observed jump in the CO_2 mixing ratio was probably due to both vertical and horizontal advection but also due to the decreased ABL depth.

5.2.3 CO_2 mixing ratio uncertainties

Sensitivity of CO_2 mixing ratio to uncertainties in the CBL variables is analyzed also for the second day in order to illustrate the differences between the two days. The initial and prescribed values used in the sensitivity analysis were the same as in Table 5.3 but with $A_c = 14 \cdot 10^{-4}\,\mathrm{ppm\,s^{-1}}$ and $\overline{w'c'}|_s = 0.25\,\mathrm{ppm\,m\,s^{-1}}$ constant in time. Time evolution of the errors in the CO_2 mixing ratio due to errors in different CBL variables are plotted in Figure 5.25 for 12th March 2004. The errors of the different variables used in the calculation are shown in

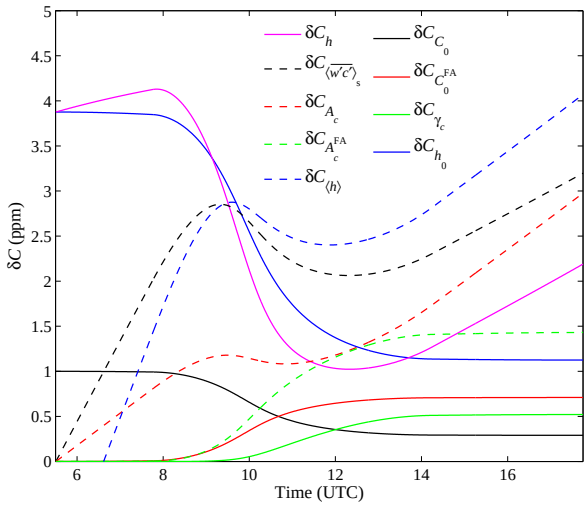

Figure 5.25: Errors in the CO_2 mixing ratio due to errors in different CBL variables on 12th March 2004. Errors used in the calculation are shown in Table 5.2.

Table 5.2. The largest errors at the end of day are due to past errors in the CBL depth and also due to the errors in the CO_2 surface flux. This is different from the first analyzed day for which the advection in the CBL was the most important source of error at the end of the day. Nevertheless, the errors in the CBL advection cause large CO_2 mixing ratio uncertainties also on the second day which implies that the previous conclusions regarding the importance of advection were not limited to the specific atmospheric conditions on the first day.

Time evolution of the CO_2 mixing ratio uncertainty due to the past errors in the CBL depth is shown in Figure 5.26 for 12th March 2004. Red circles show the error calculated from equation (5.2) with δh being the difference between the simulated and observed depths of the CBL and $A_c = 14 \cdot 10^{-4}\,\mathrm{ppm\,s^{-1}}$ constant in time. Green dashed line shows the corresponding error when δh is 100 meters and constant in time. In both cases the errors are much larger on this day than on 25th September 2003 (see Figure 5.9). This is because advection was larger and CBL shallower on 12th March 2004. Besides the period between 9:30 UTC and 10:30 UTC, the errors shown in Figure 5.26 are overestimated since a maximum value of CO_2 advection was used during the whole day. The maximum occuring around 9:30 UTC is however not overestimated. This shows that the past errors in the CBL depth can indeed cause significant error on the CO_2 mixing ratio even on a diurnal time scales.

5.2.4 Inferred CO_2 surface flux uncertainties

Time evolution of the errors in the inferred CO_2 surface flux due to errors shown in Table 5.2 are plotted in Figure 5.27 for 12th March 2004. Errors are generally of the same order than on the first day but there are differences in the relative

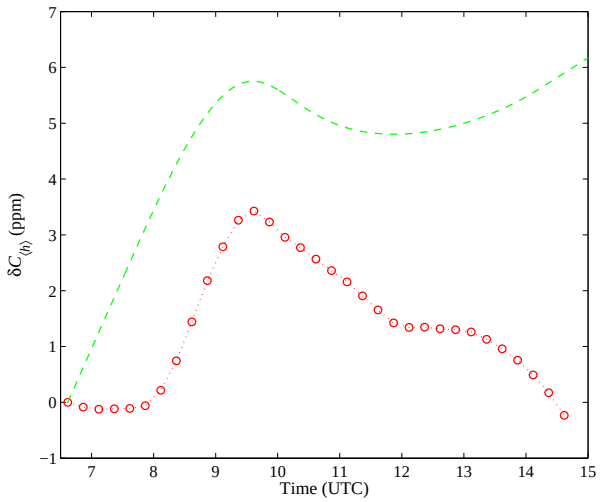

Figure 5.26: Error in the CO_2 mixing ratio due to the past uncertainties in the CBL depth on 12th March 2004. Dashed line is the CO_2 uncertainty in the case with constant error of 100 meters in the CBL depth. Red circles show the CO_2 mixing ratio uncertainty when the CBL depth error is calculated as the difference between the observed and simulated values.

significance of different errors. For example, the past errors in the CBL depth causes the largest errors after about 10 UTC since the prescribed advection was large on this day. Moreover, the uncertainty due to instantaneous CBL depth is also much larger compared to the first day due to the relatively shallow CBL. Errors in advection lead to notable errors in the inferred CO_2 surface flux in the end of day even though the CBL depth is shallow. This suggests that an erroneous estimate of advection can have non-neglibible influence on the inferred CO_2 regardless of the studied CBL.

Uncertainty of the inferred CO_2 surface flux due to the past errors in the CBL depth is plotted in Figure 5.28 for 12th March 2004. Red circles show the error calculated from equation (5.4) with δh being the difference between the simulated and observed depths of the CBL and $A_c = 14 \cdot 10^{-4}\,\mathrm{ppm\,s^{-1}}$ constant in time. Green dashed line shows the corresponding error when δh is 100 meters and constant in time. The errors are larger on this day than on 25th September 2003. The relative errors are about the same on both days, even though the errors in Figure 5.28 are overestimated due to the constant CO_2 advection.

Potential temperature and CBL depth evolutions were quite different on the two studied day but the relative sensitivities remained moderately similar (not shown). This indicates that the main conclusions about the sensitivities and their relative magnitudes given in the previous section for the 25th September 2003 should be quite general and applicable also on other convective days.

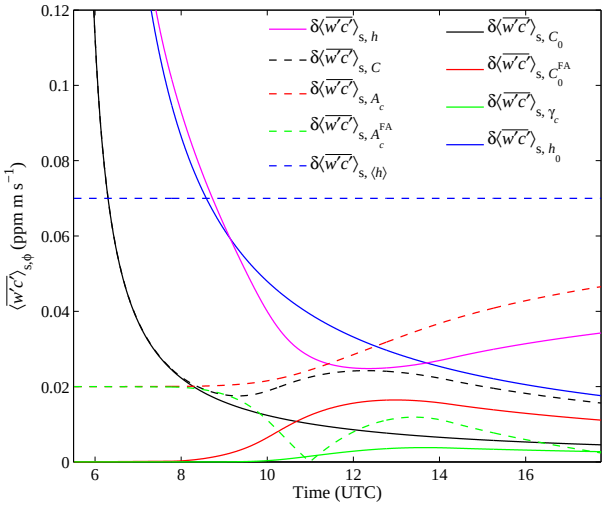

Figure 5.27: Errors in the inferred CO_2 surface flux due to errors in different variables on 12th March 2004. Errors used in the calculation are shown in Table 5.2.

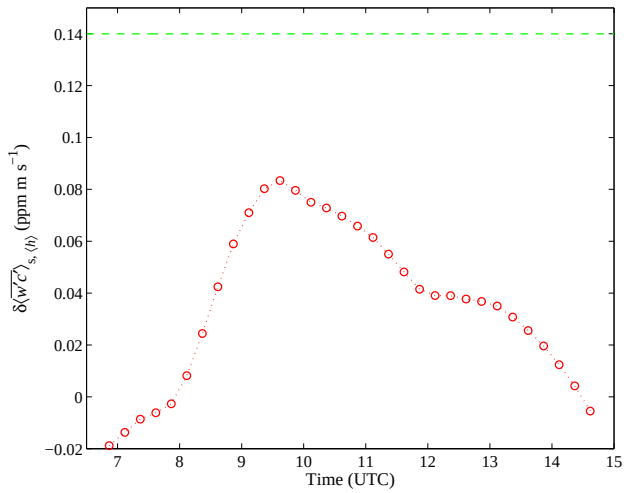

Figure 5.28: Error in the inferred CO_2 surface flux due to the past uncertainties in the CBL depth on 12th March 2004. Dashed line is the uncertainty in the case with constant error of 100 meters in CBL depth. Red circles show the inferred CO_2 surface flux uncertainty when the CBL depth error, δh, is calculated as the difference between the observed and simulated values.

Chapter 6

Summary and conclusions

In this thesis the contribution of different BL variables on the diurnal evolution of CO_2 mixing ratio and on the inferred CO_2 surface flux was studied by including horizontal CO_2 advection in the MLM based sensitivity analysis developed by Pino *et al.* [32]. This sensivity analysis was then applied to two convective days. Results of this analysis indicate that the diurnal evolution of CO_2 mixing ratio is mainly determined by the initial CO_2 mixing ratio in the BL and in the FA. Relative errors in different BL variables can however be really different and therefore the errors in nearly all BL variables can cause non-negligible uncertainties in the CO_2 mixing ratio and in the inferred CO_2 surface flux. Especially, the errors in horizontal advection can lead to notable uncertainties in the simulated CO_2 mixing ratio even on diurnal time scales. This is due to the fact that errors in horizontal advection are often large compared to errors in other CBL variables. Furthermore, CO_2 mixing ratio errors due to advection are history dependent and hence even small systematic errors can build up to cause substantial errors in the CO_2 mixing ratio. Similar conclusions can also be drawn regarding to the inferred CO_2 surface flux. These results hence implicate that advection should be carefully considered even when diurnal time scales are studied. The influence of initial inversion strength and FA potential temperature lapse rate on the sensitivities was also studied. This study could help to identify the days that are more sensitive to errors in CO_2 advection.

Uncertainties in the CO_2 mixing ratio and in the inferred CO_2 surface flux due to errors in large scale subsidence were also briefly investigated. Analytical sensitivities could not be written down but the magnitude of uncertainties in the CO_2 mixing ratio due to plausible errors in subsidence was demonstrated by numerical experiments. These results illustrates that an erroneous estimation of large scale subsidence can also lead to notable uncertainties in the simulated CO_2 mixing and in the inferred CO_2 surface flux.

Vertical advection could not be included in the MLM framework since MLM assumes constant vertical CO_2 profile in the CBL. Subsidence however changes the entrainment between the CBL and the FA, and sometimes this effect is referred as large scale vertical advection [80]. In general, it is justified to talk about advection in this context since subsiding air from the FA is advected to CBL across the entrainment zone where a vertical CO_2 gradient exists. In the case of zeroth-order MLM it is however questionable to talk about advection since the entrainment zone is infinitesimally thin and consequently, the CO_2 gra-

dient is infinite. Nevertheless, if the entrainment due to subsidence is accounted as advection, it can be considered that the influence of large scale vertical advection on the CO_2 mixing ratio evolution was also covered in the analysis. The disadvantage of this subsidence, or vertical advection, analysis is however the absence of analytical sensitivity equations. This makes it difficult to quantify the contribution of vertical advection compared to the other variables. At the same time, considering only one of the two advection terms in the CO_2 simulations and in the biosphere-atmosphere CO_2 exchange calculations would also be inappropriate [81]. For example, in heterogeneous terrain horizontal and vertical advection are closely connected and can have similar magnitudes [82–85].

Simulations of CO_2 mixing ratios and estimations of inferred CO_2 surface fluxes usually cover monthly, seasonal or annual time scales. One major drawbacks of the analysis presented in this thesis is that it only accounts for daytime evolution of the BL. MLM cannot describe stable ABLs occuring during the nights and therefore, the ML equations cannot be just integrated over long time periods. The importance of different processes on the CO_2 evolution is expected to significantly change on longer time scales. Williams *et al.* [80] showed that on long time scales the storage and entrainment become increasingly insignificant compared to the surface flux and advection. Due to this reason entrainment or storage are sometimes neglected [86, 87] when longer time scales are of interest. This approximation is commonly referred as an equilibrium approximation. On shorter time scales a non-equilibrium approximation is sometimes used which neglects the advection terms [25]. Short term and long term behaviour are thus quite opposite which emphasizes that it is not appropriate to simply apply the diurnal analysis to longer time scales. The analysis presented in this thesis can however be used to make better estimations about the applicability of non-equilibrium approximation during the day that is investigated.

In a future work the MLM will be coupled to a simple nocturnal ABL model so that longer time scales could be analyzed. Coupling the MLM with radiation and land surface models [55, 88] could also allow the study of longer time scales. Furthermore, it would be useful to consider time dependent advection which evolution would depend on the horizontal wind velocity. Horizontal wind can be easily included in the MLM but it was not considered in this work since simple sensitivity equations are no longer obtained with wind dependent advection.

The influence of convective clouds on the mixing and transport of CO_2 would also require further studies so that the parametrizations in the transport models could be improved [80]. Moreover, advection in the FA is not generally included in the MLM so it would be interesting to study in more detail the required conditions for the FA advection to occur and to have notable effects on the ABL CO_2 concentrations on diurnal or longer time scales. Convective clouds could well be connected to advection in the FA since they enhance the transport between the CBL and the FA, thus possibly creating horizontal CO_2 gradients in the FA.

Appendix A

Mixed-layer equations

By combining equations (2.25) and (2.26), the ML equations for potential temperature, specific humidity and CO_2 mixing ratio reads:

$$\frac{\partial \theta_{\mathrm{ml}}}{\partial t} = \frac{1}{h}\left[\overline{w'\theta'}|_{\mathrm{s}} + \Delta\theta\left(\frac{\partial h}{\partial t} - w_{\mathrm{s}}\right)\right] + A_\theta \tag{A.1}$$

$$\frac{\partial q_{\mathrm{ml}}}{\partial t} = \frac{1}{h}\left[\overline{w'q'}|_{\mathrm{s}} + \Delta q\left(\frac{\partial h}{\partial t} - w_{\mathrm{s}}\right)\right] + A_q \tag{A.2}$$

$$\frac{\partial C_{\mathrm{ml}}}{\partial t} = \frac{1}{h}\left[\overline{w'c'}|_{\mathrm{s}} + \Delta C\left(\frac{\partial h}{\partial t} - w_{\mathrm{s}}\right)\right] + A_c \tag{A.3}$$

In addition, the ML equations for $\Delta\theta$, Δq and ΔC reads:

$$\frac{\partial \Delta\theta}{\partial t} = \gamma_\theta\left(\frac{\partial h}{\partial t} - w_{\mathrm{s}}\right) A_\theta^{\mathrm{FA}} - \frac{\partial \theta_{\mathrm{ml}}}{\partial t} \tag{A.4}$$

$$\frac{\partial \Delta q}{\partial t} = \gamma_q\left(\frac{\partial h}{\partial t} - w_{\mathrm{s}}\right) A_q^{\mathrm{FA}} - \frac{\partial q_{\mathrm{ml}}}{\partial t} \tag{A.5}$$

$$\frac{\partial \Delta C}{\partial t} = \gamma_c\left(\frac{\partial h}{\partial t} - w_{\mathrm{s}}\right) A_C^{\mathrm{FA}} - \frac{\partial C_{\mathrm{ml}}}{\partial t} \tag{A.6}$$

Furthermore, the evolution of the CBL growth is given by:

$$\frac{\partial h}{\partial t} = -\frac{\overline{w'\theta'_{\mathrm{v}}}|_{\mathrm{e}}}{\Delta\theta_{\mathrm{v}}} + w_{\mathrm{s}} \tag{A.7}$$

To close the system of ML equations an assumption is made which describes the entrainment buoyancy flux as a constant fraction of the surface buoyancy flux:

$$\overline{w'\theta'_{\mathrm{v}}}|_{\mathrm{e}} = -\beta_{\theta_{\mathrm{v}}}\overline{w'\theta'_{\mathrm{v}}}|_{\mathrm{s}} \tag{A.8}$$

Appendix B

Derivation of the relation between h and h_0

Subsidence and advection of heat and moisture are neglected in the following derivation. By using the chain rule equation (A.4) can then be written as

$$\frac{\partial \Delta\theta}{\partial t} = \frac{\partial \Delta\theta}{\partial h}\frac{\partial h}{\partial t} = \gamma_\theta \frac{\partial h}{\partial t} - \frac{\partial \theta_{\mathrm{ml}}}{\partial h}\frac{\partial h}{\partial t}\,. \tag{B.1}$$

Equation (B.1) is then divided by $\frac{\partial h}{\partial t}$ leading to

$$\frac{\partial \Delta\theta}{\partial h} = \gamma_\theta - \frac{1+\beta}{\beta}\frac{\partial \theta_{\mathrm{ml}}}{\partial h} \tag{B.2}$$

The last term on the RHS of this equation is obtained from equations (A.7) and (A.1). First, equation (A.1) is written as

$$\frac{\partial \theta_{\mathrm{ml}}}{\partial t} = \frac{\partial \theta_{\mathrm{ml}}}{\partial h}\frac{\partial h}{\partial t} = (1+\beta)\frac{\overline{w'\theta'}|_s}{h}\,. \tag{B.3}$$

Next, equation (A.7) is substituted into (B.1) and the terms are rearranged so that an expression for the last term of equation (B.2) is obtained:

$$\frac{\partial \theta}{\partial h} = \frac{1+\beta}{\beta}\frac{\Delta\theta}{h}\,. \tag{B.4}$$

Plugging the results into (B.2) gives

$$\frac{\partial \Delta\theta}{\partial h} = \gamma_\theta - \frac{1+\beta}{\beta}\frac{\Delta\theta}{h}\,. \tag{B.5}$$

Solution of (B.5) is given by

$$\Delta\theta = B_0 h^a + \frac{\gamma_\theta h}{1+a}\,, \tag{B.6}$$

where

$$a = \frac{1+\beta}{\beta} \tag{B.7}$$

and

$$B_0 = \left(\Delta\theta_0 - \frac{\gamma_\theta h_0}{1+a}\right) h_0^a \tag{B.8}$$

with $\Delta\theta_0$ being the initial inversion strength.

Next, equation (A.7) is multiplied by $\Delta\theta$ resulting in

$$\Delta\theta \frac{\partial h}{\partial t} = \beta\, \overline{w'\theta'}|_s \,. \tag{B.9}$$

Substituting $\Delta\theta$ from equation (B.5) to (B.9) and integrating from t_0 to t gives

$$\int_{h_0}^{h} \left(B_0 h^a + \frac{\gamma_\theta h}{1+a}\right) \mathrm{d}h = \beta \int_{t_0}^{t} \overline{w'\theta'}|_s \mathrm{d}t \,, \tag{B.10}$$

where $h_0 = h(t_0)$. Performing the integration on the RHS gives

$$B_1 h^{1-a} + B_2 h^2 - B_3 = \beta \int_{t_0}^{t} \overline{w'\theta'}|_s \mathrm{d}t \,, \tag{B.11}$$

where

$$B_1 = \frac{B_0}{1-a} \,, \tag{B.12}$$

$$B_2 = \frac{\gamma_\theta}{2(1+a)} \,, \tag{B.13}$$

and

$$B_3 = \frac{B_0}{1-a} h_0^{1-a} + \frac{\gamma_\theta}{2(1+a)} h_0^2 \,. \tag{B.14}$$

By taking partial derivatives from both sides of equation (B.11) with respect to h_0 we get

$$h^{1-a} \frac{\partial B_1}{\partial h_0} + (1-a) h^{-a} B_1 \frac{\partial h}{\partial h_0} + 2 B_2 h \frac{\partial h}{\partial h_0} = \frac{\partial B_3}{\partial h_0} \,. \tag{B.15}$$

Finally solving this with respect to $\frac{\partial h}{\partial h_0}$ leads to the desired solution

$$\frac{\partial h}{\partial h_0} = \frac{\frac{\partial B_3}{\partial h_0} - \frac{\partial B_1}{\partial h_0} h^{1-a}}{B_1 (1-a) h^{-a} + 2 B_2 h} \,, \tag{B.16}$$

where

$$\frac{\partial B_1}{\partial h_0} = \frac{a \Delta\theta_0}{1-a} h_0^{a-1} - \frac{\gamma_\theta}{1-a} h_0^a \tag{B.17}$$

and

$$\frac{\partial B_3}{\partial h_0} = \frac{\Delta\theta_0}{1-a} - \frac{2\gamma_\theta}{1-a^2} h_0 + \frac{\gamma_\theta}{1+a} h_0 \,. \tag{B.18}$$

Appendix C

List of symbols and acronyms

CO_2	carbon dioxide
ABL	atmospheric boundary layer
CBL	convective boundary layer
ML	mixed-layer
FA	free atmosphere
MLM	mixed-layer model
MM5	The fifth-generation Pennsylvania State University - National Center of Atmospheric Research Mesoscale Model
q_t	total specific humidity
m_w	mass of water in a parcel of air
m	total mass of a parcel of air
m_v	mass of water vapour in a parcel of air
m_l	mass of liquid water in a parcel of air
m_i	mass of ice in a parcel of air
m_d	mass of a parcel of dry air
ρ (ρ_d)	density of moist (dry) air
V	volume of a parcel of air
q_v	mass fraction of water vapour
$p\,(p_\mathrm{i})$	total (partial) pressure
$R_\mathrm{m}\,(R_\mathrm{d})$	gas constant of moist (dry) air
R_v	gas constant of water vapour
T	absolute temperature
T_v	virtual temperature
θ	potential temperature
p_0	standard pressure
Q	thermal energy
α	specific volume
c_p	specific heat at constant pressure
s	specific entropy
θ_v	virtual potential temperature
φ	scalar variable
$\overline{\varphi}\,(\varphi')$	mean (fluctuation) of φ

t	time
x_j	Cartesian coordinate, $\vec{x} = (x, y, z)$
u_j	component of wind velocity, $\vec{u} = (u, v, w)$
RHS	right hand side
g	acceleration of gravity
δ_{ij}	Kronecker delta
ω	angular velocity of Earth's rotation
Ω_j	component of angular velocity vector
λ	latitude
ϵ_{ijk}	Levi-Civita
τ_{ij}	shear stress tensor
S_φ	Sources and sinks of scalarφ
φ_{ml}	ML value of variable φ
h	depth of the boundary layer
z_0	surface roughness length
$\overline{w'\varphi'}\vert_{\mathrm{s}}$	vertical turbulent flux of φ at surface
$\overline{w'\varphi'}\vert_{\mathrm{e}}$	vertical turbulent flux of φ at the top of the ML
φ^{FA}	value of $\overline{\varphi}$ in the FA just above the inversion
$\Delta\varphi$	difference between φ_{ml} and φ^{FA}
w_{e}	entrainment velocity
ω_{s}	large scale divergence
γ_φ	vertical gradient of $\overline{\varphi}$ in the FA
A_φ (A_φ^{FA})	advection of $\overline{\varphi}$ in the ML (in the FA)
$\beta_{\theta_{\mathrm{v}}}$	ratio of entrainment flux of θ_{v} to surface flux of θ_{v}
ECMWF	European Center for Medium-Range Weather Forecasts
C	CO_2 mixing ratio
h_0 (t_0)	initial BL depth (time) in the ML simulations
C_0	initial CO_2 mixing ratio in the ML
C_0^{FA}	initial CO_2 mixing ratio in the FA just above the ML
$\langle\overline{w'c'}\rangle_{\mathrm{s}}$	time averaged CO_2 surface turbulent flux
$\delta\phi$	error in variable ϕ
UTC	Coordinated Universal Time
$\Delta\varphi_0$	initial $\Delta\varphi$ in the ML simulations
RSC_ϕ	relative sensitivity of C_{ml} to variable ϕ
$\delta\langle h\rangle$	time averaged error in the BL depth
RSF_ϕ	relative sensitivity of $\langle\overline{w'c'}\rangle_{\mathrm{s}}$ to variable ϕ
NEE	net ecosystem-atmosphere exchange
IU	height integral of horizontal wind speed
z_1, z_2	vertical limits of integration in IU
a	coefficient
B_0, B_1, B_2, B_3	coefficients

Bibliography

[1] R. B. Stull, *An Introduction to Boundary Layer Meteorology* (Kluwer Academic Publisher, Amsterdam, 1988).

[2] J. M. Wallace and P. V. Hobbs, *Atmospheric Science: An Introductory Survey, 2nd ed.* (Academic Press, New York, 2006).

[3] A. G. M. Driedonks and H. Tennekes, Bound.-Layer Meteor. **30**, 75 (1984).

[4] C. D. Keeling and T. P. Whorf, Atmospheric CO_2 records from sites in the SIO air sampling network. Trends '93: A compedium of data on global change., Oak Ridge National Laboratory Rep. ORNL/CDIAC-65, 16-26, 1994.

[5] T. J. Conway, P. P. Tans, L. S. Waterman, K. W. Thoning, D. R. Kitzis, K. Masarie and N. Zhang, J. Geophys. Res. **99**, 22831 (1994).

[6] J. Houghton, Int. J. Environ. Pollut. **3(1-3)**, 7 (1993).

[7] P. Cox, R. Betts, C. Jones, S. Spall, and I. Totterdell, Nature **408**, 184 (2000).

[8] A. Rörsch, R. Courtney, and D. Thoenes, Energy Environ. **16**, 217 (2005).

[9] H. Le Treut, R. Somerville, U. Cubasch, Y. Ding, C. Mauritzen, A. Mokssit, T. Peterson, and M. Prather, Historical Overview of Climate Change, Climate Change 2007: The Physical Science Basis. Contribution of Working Group I to the Fourth Assessment Report of the Intergovernmental Panel on Climate Change, 2007.

[10] D. Baldocchi, E. Falge, L. Gu, R. Olson, D. Hollinger, S. Running, P. Anthoni, C. Bernhofer, K. Davis, R. Evans, J. Fuentes, A. Goldstein, G. Katul, B. Law, X., Lee, Y. Malhi, T. Meyers, W. Munger, W. Oechel, K. T. Paw U, K. Pilegaard, H. P. Schmid, R. Valentini, S. Verma, T. Vesala, K. Wilson and S. Wofsy, Bull. Amer. Soc. **82**, 2416 (2001).

[11] M. Aubinet, A. Grelle, A. Ibrom, Ü. Rannik, J. Moncrieff, T. Foken, A. S. Kowalski, P. H. Martin, P. Berbigier, C. Bernhofer, R. Clement, J. Elbers, A. Granier, T. Grünwald, K. Morgenstern, K. Pilegaard, C. Rebmann, W. Snijders, R. Valentini and T. Vesala, Adv. Ecol. Res. **30**, 113 (2000).

[12] R. Valentini, G. Matteucci, A. J. Dolman, E.-D. Schulze, C. Rebmann, E. J. Moors, A. Granier, P. Gross, N. O. Jensen, K. Pilegaard, A. Lindroth, A. Grelle, C. Bernhofer, T. Grünwald, M. Aubinet, R. Ceulemans, A. S. Kowalski, T. Vesala, Ü. Rannik, P. Berbigier, D. Loustau, J. Guðmundsson, H. Thorgeirsson, A. Ibrom, K. Morgenstern, R. Clement, J. Moncrieff, L. Montagnani, S. Minerbi and P. G. Jarvis, Nature **404**, 861 (2000).

[13] T. L. Crawford, R. J. Dobosy, R. T. McMillen, C. A. Vogel and B. B. Hicks, Global Change Biol. **2**, 275 (1999).

[14] R. L. Desjardins, J. I. MacPherson, L. Mahrt, P. Schuepp, E. Pattey, H. Neumann, D. Baldocchi, S. Wofsy, D. Fitzjarrald, H. McCaughey and D. W. Joiner, J. Geophys. Res. **102**, 29, 125 (1997).

[15] O. T. Denmead, M. R. Raupach, F. X. Dunin, H. A. Cleugh and R. Leuning, Global Change Biol. **2**, 255 (1996).

[16] A. S. Denning, J. G. Collatz, C. Zhang, D. A. Randall, J. A. Berry, P. J. Sellers, G. D. Colello and D. A. Dazlich, Tellus **48B**, 521 (1996).

[17] S. M. Fan, M. Gloor, J. Mahlman, S. Pacala, J. Sarmiento, T. Takahashi and P. Tans, Science **282**, 442 (1998).

[18] P. P. Tans, I. Y. Fung and T. Takahashi, Science **247**, 1431 (1990).

[19] K. R. Gurney, R. M. Law, A. S. Denning, P. J. Rayner, D. Baker, P. Bousquet, L. Bruhwiler, Y. H. Chen, P. Ciais, S. Fan, I. Y. Fung, M. Gloor, M. Heimann, K. Higuchi, J. John, T. Maki, S. Maksyutov, K. Masarie, P. Peylin, M. Prather, B. C. Pak, J. Randerson, J. Sarmiento, S. Taguchi, T. Takahashi, and C. W. Yuen, Nature **415(6872)**, 626 (2003).

[20] C. D. Keeling S. C. Piper, T. P. Whorf and R. F. Keeling, Tellus Ser. B **63**, 1 (2011).

[21] A. R. Desai, B. R.Helliker, P. R. Moorcroft, A. E. Andrews and J. A. Berry, J. Geophys. Res. **115**, G02011 (2010).

[22] A. D. Culf, G. Fisch, G. Y. Malhi, and C. A. Nobre, Agri. Forest Meteorol. **85**, 149 (1997).

[23] C. M. J. Jacobs and H. A. R. De Bruin, J. Appl. Meteorol. **36**, 1663 (1997).

[24] C. Yi, K. J. Davis, B. W. Berger and P. S. Bakwin, J. Atmos. Sci. **58**, 1288 (2001).

[25] C. Yi, K. J. Davis, P. S. Bakwin, A. S. Denning, N. Zhang, A. Densai, J. C. Lin and C. Gerbig, J. Geophys. Res.-Atmos. **109**, D08302 (2004).

[26] J. Vilà-Guerau de Arellano, B. Gioli, F. Miglietta, H. Jonker, H., H. Baltink, R. Hutjes and A. Holtslag, J. Geophys. Res. **109**, D18110 (2004).

[27] J. Lloyd, O. Kolle, H. Fritsch, S. R. de Freitas, M. A. F. Silva Dias, P. Artaxo, A. D. Nobre, A. C. de Ara*ú*jo, B. Kruijt, L. Sogacheva, G. Fisch, A. Thielmann, U. Kuhn and M. O. Andreae, Biogeosci. **4**, 759 (2007).

[28] P. Casso-Torralba, J. Vilà-Guerau de Arellano, F. Bosveld, M. R. Soler, A. Vermeulen, C. Werner, and E. Moors, J. Geophys. Res. **113**, D12119 (2008).

[29] E. McGrath-Spangler and S. Denning, Tellus B **62**, 441 (2010).

[30] A. S. Denning, I. Y. Fung and D. Randall, Nature **376**, 240 (1995).

[31] S. C. Wofsy, R. C. Harriss and W. A. Kaplan, J. Geophys. Res. **93**, 1377 (1988).

[32] D. Pino, J. Vilà-Guerau de Arellano, W. Peters, J. Schroter, C. C. van Heerwaarden, and M. Krol, Atmos. Chem. Phys. Discuss. **11**, 32769 (2011).

[33] D. K. Lilly, Quart. J. Roy. Meteorol. Soc. **94**, 292 (1968).

[34] A. K. Betts, Q. J. R. Meteorol. Soc. **99**, 178 (1973).

[35] D. J. Carson, Quart. J. Roy. Meteor. Soc. **99**, 450 (1973).

[36] H. Tennekes, Atmos. Sci. **30**, 558 (1973).

[37] H. Tennekes and A. G. M. Driedonks, Bound.-Lay. Meteorol. **20**, 515 (1981).

[38] J. Dudhia, J. Atmos. Sci. **46**, 3077 (1989).

[39] J. A. Dutton and G. H. Frichtl, J. Atmos. Sci. **26**, 241 (1969).

[40] J. A. Businger, in *Equations and concepts. Chapt. 1 in Atmospheric Turbulence and Air Pollution Modelling*, edited by F. T. M. Nieuwstadt and H. van Dop (Reidel Publishing Co., Dordrecht, 1982).

[41] L. Mahrt and D. H. Lenschow, J. Atmos. Sci. **33**, 41 (1976).

[42] J. W. Deardorff, G. E. Willis and B. H. Stockton,, J. Fluid Mech. **100**, 41 (1980).

[43] S.-W. Kim, D. Pino, and J. Vilà-Guerau de Arellano, Bound.-Layer Meteor. **120**, 455 (2006).

[44] R. T. Pollard, P. B. Rhines and R. O. R. Y. Thompson, Geophys. Fluid Dyn. **3**, 381 (1973).

[45] P. P. Niiler, J. Marine Res. **33**, 405 (1975).

[46] P. P. Niiler and E. B. Kraus, *One-dimensional models of the upper ocean*, (Modelling and prediction of the upper layers of the ocean, Pergamon Press, Oxford, 1977).

[47] P. P. Niiler, *One-dimensional models of the seasonal thermocline*, (The Sea, Vol. 6, Wiley, New York, 1977).

[48] A. G. M. Driedonks, Ph.D. thesis, Vrije Universiteit te Amsterdam, 1981.

[49] J. Vilà-Guerau de Arellano and C. C. van Heerwaarden, *Cloud formation: clear to cloudy atmospheric boundary layers*, Meteorology and Air Quality Section, Wageninged University, The Netherlands, 2011.

[50] G. I. Taylor, Proc. R. Soc. **A164**, 476 (1938).

[51] K. J. Davis, Ph.D. thesis, University of Colorado, Boulder, 1992.

[52] C. Yi, K. J. Davis, P. S. Bakwin and L. C. Marr, J. Geophys. Res. **105**, D8, 9991 (2000).

[53] P. Seibert, F. Beyrich, S.-E. Gryning, S. Joffre, A. Rasmussen and P. Tercier, Atmos. Env. **34**, 1001 (2000).

[54] A. K. Betts, J. Geophys. Res. **97**, 523 (1992).

[55] C. C. van Heerwaarden, J. Vilà-Guerau de Arellano, A. Gounou, F. Guichard and F. Gouvreux, J. Hydrometeor. **11**, 1405 (2010).

[56] C. C. van Heerwaarden, Ph.D. thesis, Wageningen University, 2011.

[57] O. Zeman and H. Tennekes, J. Atmos. Sci. **34**, 112 (1977).

[58] H. Tennekes, J. Atmos. Sci. **32**, 992 (1975).

[59] D. Pino, J. Vilà-Guerau de Arellano and P. G. Duynkerke, J. Atmos. Sci. **60**, 1913 (2003).

[60] R. J. Conzemius and E. Fedorovich, J. Atmos. Sci. **63**, 1151 (2006).

[61] R. J. Conzemius and E. Fedorovich, J. Atmos. Sci. **63**, 1179 (2006).

[62] F. K. Ball, Quart. J. Roy. Meteor. Soc. **80**, 483 (1960).

[63] K. A. Emanuel, *Forced and free mesoscale motions in the atmosphere*, Proceedings of the CIMMS Symposium, Norman, OK, May 12-16, 1982.

[64] R. A. Pielke, *Mesoscale Meteorological Modeling. 2nd edition* (Academic Press, San Diego, CA, 2002).

[65] J. S. Kain and J. M. Fritsch, Meteor. Monogr., No. 24, Amer. Meteor. Soc. 165 (1993).

[66] S.-Y. Hong and H.-L. Pan, Mon. Wea. Rev. **124**, 2322 (1996).

[67] R. D. Pyles, B. C. Weare, K. T. Paw and W. Gustafson, J. Appl. Meteor. **42**, 557 (2003).

[68] Y. Liu, J. H. He, W. L. Li and L. X. Chen, Acta Meteorol. Sin. **22**, 8 (2008).

[69] C. M. J. Jacobs and H. A. R. De Bruin, J. Clim. **5**, 683 (1992).

[70] A. Van Ulden and J. Wieringa, Bound.-Lay. Meteorol. **78**, 39 (1996).

[71] A. C. M. Beljaars and F. C. Bosveld, J. Climate **10**, 1172 (1997).

[72] C, F, Bosveld, A. Vermeulen and E. Moors, The role of advection on CO_2 flux measurements at the Cabauw tall tower, The Netherlands, 17th Symposium on Boundary Layers and Turbulence, 2006.

[73] A. T. Vermeulen, A. Hensen, M. E. Popa, W. C. M. van den Bulk, and P. A. C. Jongejan, Atmos. Meas. Tech. **4**, 617 (2011).

[74] W. Kohsiek, J. Atmos. Ocean. Tech. **17(3)**, 299 (2000).

[75] F. C. Bosveld, E. van Meijgaard, E. Moors and C. Werner, Interpretation of flux observations along the Cabauw 200 m meteorological tower, 16th Symposium on Boundary Layers and Turbulence, 2004.

[76] A. G. M. Driedonks, Bound.-Layer Meteor. **23**, 283 (1982).

[77] C. Chan, C. W. Yuen, K. Higuchi, A. Shashkov, J. Liu, J. Chen and D. Worthy, Tellus **56B**, 194 (2004).

[78] NERC Satellite Receiving Station, Dundee University, Scotland, `http://www.sat.dundee.ac.uk/`, accessed: 1.11.2011.

[79] J. L. Sun and L. Mahrt, J. Appl. Meteorol. **33**, 1341 (1994).

[80] I. N. Williams, W. J. Riley, M. S. Torn, J. A. Berry and S. C. Biraud, Atmos. Chem. Phys. **11**, 9631 (2011).

[81] W. Wang, K. J. Davis, B. D. Cook, P. S. Bakwin, C. Yi, M. P. Butler and D. M. Ricciuto, Agr. Forest Meteorol. **135**, 202 (2005).

[82] J. Finnigan, Agric. For. Meteorol. **97**, 55 (1999).

[83] J. Sun, D. H. Lenschow, L. Mahrt, T. L. Crawford, K. J. Davis, S. P. Oncley, J. I. MacPherson, Q. Wang, R. J. Dobosy and R. L. Desjardins, J. Geophys. Res. **102**, 155 (1997).

[84] J. Sun, R. Desjardins, L. Mahrt and I. MacPherson, J. Geophys. Res. **103**, 873 (1998).

[85] L. Mahrt, J. Sun, D. Vickers, J. I. MacPherson and R. L. Dejardins, J. Atmos. Sci. **51**, 2484 (1994).

[86] P. S. Bakwin, K. J. Davis, C. Yi, S. C. Wofsy, J. W. Munger, L. Haszpra and Z. Barcza, Tellus B - Chem. Phys. Meteorol. **56**, 301 (2004).

[87] B. R. Helliker, J. A. Berry, A. K. Betts, P. S. Bakwin, K. J. Davis, A. S. Denning, J. R. Ehleringer, J. B. Miller, M. P. Butler and D. M. Ricciuto, J. Geophys. Res.-Atmos. **109**, D20106 (2004).

[88] C. C. van Heerwaarden, J. Vilà-Guerau de Arellano, A. F. Moene and A. A. M. Holtslag, Quart. J. Roy. Meteor. Soc. **135**, 1277 (2009).